UNIVERSITY OF AMSTERDAM

UvA-DARE (Digital Academic Repository)

# A probe of the maximum energetics of fast radio bursts through a prolific repeating source

Ould-Boukattine, O.S.; Chawla, P.; Hessels, J.W.T.; Cooper, A.J.; Gawroński, M.P.; Herrmann, W.; Hewitt, D.M.; Huang, J.; Huppenkothen, D.; Kirsten, F.; Konijn, D.C.; Nimmo, K.; Pleunis, Z.; Puchalska, W.; Snelders, M.P.

**DOI**
10.1093/mnras/staf1937

**Publication date**
2026

**Document Version**
Final published version

**Published in**
Monthly Notices of the Royal Astronomical Society

**License**
CC BY

Link to publication

**Citation for published version (APA):**
Ould-Boukattine, O. S., Chawla, P., Hessels, J. W. T., Cooper, A. J., Gawroński, M. P., Herrmann, W., Hewitt, D. M., Huang, J., Huppenkothen, D., Kirsten, F., Konijn, D. C., Nimmo, K., Pleunis, Z., Puchalska, W., & Snelders, M. P. (2026). A probe of the maximum energetics of fast radio bursts through a prolific repeating source. *Monthly Notices of the Royal Astronomical Society*, *545*(2), Article staf1937. https://doi.org/10.1093/mnras/staf1937

**General rights**
It is not permitted to download or to forward/distribute the text or part of it without the consent of the author(s) and/or copyright holder(s), other than for strictly personal, individual use, unless the work is under an open content license (like Creative Commons).

**Disclaimer/Complaints regulations**
If you believe that digital publication of certain material infringes any of your rights or (privacy) interests, please let the Library know, stating your reasons. In case of a legitimate complaint, the Library will make the material inaccessible and/or remove it from the website. Please Ask the Library: https://uba.uva.nl/en/contact, or a letter to: Library of the University of Amsterdam, Secretariat, P.O. Box 19185, 1000 GD Amsterdam, The Netherlands. You will be contacted as soon as possible.

*UvA-DARE is a service provided by the library of the University of Amsterdam (https://dare.uva.nl)*

Download date:17 Nov 2026

Monthly Notices of the ROYAL ASTRONOMICAL SOCIETY

MNRAS **545,** 1–16 (2026) https://doi.org/10.1093/mnras/staf1937
Advance Access publication 2025 November 8

# A probe of the maximum energetics of fast radio bursts through a prolific repeating source

O. S. Ould-Boukattine [1,2★] P. Chawla [1,2] J. W. T. Hessels [1,2,3,4] A. J. Cooper [5] M. P. Gawroński [6] W. Herrmann [7] D. M. Hewitt [2] J. Huang [3,4] D. Huppenkothen [2,8] F. Kirsten [1,9] D. C. Konijn [1,10] K. Nimmo [11] Z. Pleunis [1,2] W. Puchalska [6] and M. P. Snelders [1,2]

[1]*ASTRON, Netherlands Institute for Radio Astronomy, Oude Hoogeveensedijk 4, NL-7991 PD Dwingeloo, the Netherlands*
[2]*Anton Pannekoek Institute for Astronomy, University of Amsterdam, Science Park 904, NL-1098 XH Amsterdam, the Netherlands*
[3]*Trottier Space Institute, McGill University, 3550 rue University, Montréal, QC H3A 2A7, Canada*
[4]*Department of Physics, McGill University, 3600 rue University, Montréal, QC H3A 2T8, Canada*
[5]*Astrophysics, The University of Oxford, Keble Road, Oxford, OX1 3RH, UK*
[6]*Institute of Astronomy, Faculty of Physics, Astronomy and Informatics, Nicolaus Copernicus University, Grudziadzka 5, PL-87-100 Toruń, Poland*
[7]*Astropeiler Stockert e.V., Astropeiler 1-4, D-53902 Bad Münstereifel, Germany*
[8]*SRON Netherlands Institute for Space Research, Niels Bohrlaan 4, NL-2333 CA Leiden, the Netherlands*
[9]*Department of Space, Earth and Environment, Chalmers University of Technology, Onsala Space Observatory, SE-439 92, Onsala, Sweden*
[10]*Kapteyn Astronomical Institute, University of Groningen, Kapteynborg 5419, NL-9747 AD, Groningen, the Netherlands*
[11]*MIT Kavli Institute for Astrophysics and Space Research, Massachusetts Institute of Technology, 77 Massachusetts Ave, Cambridge, MA 02139, USA*

Accepted 2025 October 25. Received 2025 October 13; in original form 2025 July 30

## ABSTRACT

Fast radio bursts (FRBs) are sufficiently energetic to be detectable from luminosity distances up to at least seven billion parsecs (redshift $z > 1$). Probing the maximum energies and luminosities of FRBs constrains their emission mechanism and cosmological population. Here, we investigate the maximum energetics of a highly active repeater, FRB 20220912A, using 1500 h of observations. We detect 130 high-energy bursts and find a break in the burst energy distribution, with a flattening of the power-law slope at higher energy – consistent with the behaviour of another highly active repeater, FRB 20201124A. There is a roughly equal split of integrated burst energy between the low- and high-energy regimes. Furthermore, we model the rate of the highest energy bursts and find a turnover at a characteristic spectral energy density of $E_\nu^{\rm char} = 2.09^{+3.78}_{-1.04} \times 10^{32}\,{\rm erg\,Hz^{-1}}$. This characteristic maximum energy agrees well with observations of apparently one-off FRBs, suggesting a common physical mechanism for their emission. The extreme burst energies push radiation and source models to their limit: at this burst rate a typical magnetar ($B = 10^{15}$ G) would deplete the energy stored in its magnetosphere in ∼2150 h, assuming a radio efficiency $\epsilon_{\rm radio} = 10^{-5}$. We find that the high-energy bursts ($E_\nu > 3 \times 10^{30}\,{\rm erg\,Hz^{-1}}$) play an important role in exhausting the energy budget of the source.

**Key words:** radio continuum: transients – fast radio bursts.

## 1 INTRODUCTION

Fast radio bursts (FRBs; E. Petroff, J. W. T. Hessels & D. R. Lorimer 2022) are observed with durations ranging from microseconds (M. P. Snelders et al. 2023) to seconds (B. C. CHIME/FRB Collaboration 2022) and fluences ranging from about 0.01–1000 Jy ms (L. G. Spitler et al. 2016; F. Kirsten et al. 2024). Of the thousands of known FRBs, most are observed as one-off events and only a few per cent are known to repeat (CHIME/FRB Collaboration 2023). It remains unclear whether the repeaters and apparent non-repeaters have different astrophysical origins. An exceptionally bright (MJy) burst has been observed from the Galactic magnetar SGR 1935+2154, and strongly suggests that at least some FRBs originate from magnetars (C. D. Bochenek et al. 2020; CHIME/FRB Collaboration 2020).

Though FRB emission is almost certainly beamed, the beaming fraction is unknown. For simplicity, isotropic-equivalent energies are used to compare different FRBs even though this is an overestimation of the total energy released in radio waves. Given the typical Mpc- to Gpc-distances of FRBs (A. C. Gordon et al. 2023), their isotropic-equivalent energies are known to range from roughly $E = 10^{37}$–$10^{42}$ erg. This is at least four orders-of-magnitude larger than what is measured for Galactic radio pulsars, including the giant pulses seen from the Crab pulsar (A. Bera & J. N. Chengalur 2019). SGR 1935+2154, however, is known to produce bursts whose energies span the range between pulsars and FRBs (F. Kirsten et al. 2021 and references therein).

Furthermore, it is expected that the detected radio energy is only a small fraction (∼$10^{-5}$) of the total bolometric energy released at the source during an FRB event (B. D. Metzger, B. Margalit & L. Sironi 2019; S. Mereghetti et al. 2020). Taking this into account, the most energetic known FRBs may be associated with ∼$10^{46–47}$ erg events

★ E-mail: ouldboukattine@astron.nl

© The Author(s) 2025.
Published by Oxford University Press on behalf of Royal Astronomical Society. This is an Open Access article distributed under the terms of the Creative Commons Attribution License (https://creativecommons.org/licenses/by/4.0/), which permits unrestricted reuse, distribution, and reproduction in any medium, provided the original work is properly cited.

Downloaded from academic.oup.com/mnras/article/545/2/staf1937/8317171 by Universiteit van Amsterdam user on 09 October 2026

**Table 1.** Observational set-up.

| Station[a] | Band | Frequency [MHz] | Bandwidth[b] [MHz] | Bandwidth per subband [MHz] | SEFD[c] [Jy] | Detection[d] threshold [Jy ms] | Completeness[e] threshold [Jy ms] | Completeness[f] threshold [$10^{30}$ erg Hz$^{-1}$] | Time observed[g] [h] |
|---|---|---|---|---|---|---|---|---|---|
| Wb | $P$ | 300–356 | 50 | 8 | 2100 | 46.5 | 172.5 | 23.36 | 607.34 |
| Wb | $L_{\rm Wb}$ | 1259–1387 | 100 | 16 | 420 | 6.6 | 24.4 | 3.30 | 196.58 |
| St | $L_{\rm St}$ | 1332.5–1430.5 | 90 | 98 | 385 | 6.4 | 23.6 | 3.20 | 933.53 |
| Tr | $L_{\rm Tr-1}$ | 1290–1546 | 200 | 32 | 350 | 3.9 | 14.4 | 1.95 | 3.23 |
| Tr | $L_{\rm Tr-2}$ | 1350–1478 | 100 | 16 | 350 | 5.5 | 20.3 | 2.75 | 268.10 |
| Tr | $C_{\rm Tr-1}$ | 4550–4806 | 200 | 32 | 220 | 2.4 | 7.9 | 1.07 | 40.39 |
| Tr | $C_{\rm Tr-2}$ | 4600–4728 | 100 | 32 | 220 | 3.4 | 11.3 | 1.53 | 113.87 |
| O8 | $C_{\rm O8}$ | 4798.5–5054.5 | 200 | 32 | 480 | 5.3 | 17.4 | 2.36 | 28.36 |
| Total time at 1.4 GHz ($L$ band) on source [h][h] | | | | | | | | | 1159 |
| Total telescope time/total time on source [h][h] | | | | | | | | | 2192/1491 |

[a]Wb: Westerbork RT1, St: Stockert, Tr: Toruń, O8: Onsala 25 − m.
[b]Effective bandwidth accounting for RFI and band edges.
[c]From the EVN status page (with the exception of St).
[d]Assuming a 7$\sigma$ detection threshold and a typical FRB pulse width of 1 ms.
[e]Assuming a 15$\sigma$ detection threshold and a width of 3 ms.
[f]Fluence completeness converted using equation (1).
[g]Hours spend on source between MJD 59 867 and 59 983 (2022 October 15 and 2023 February 08).
[h]Total time on source accounts for overlap between the participating telescopes.

that are comparable to the most extreme 'giant flares' from magnetars (V. M. Kaspi & A. M. Beloborodov 2017), though still at least four orders-of-magnitude less energetic compared to supernovae and gamma-ray bursts. None the less, FRBs display extreme brightness temperatures $T_{\rm B} \gg 10^{12}$ K (the typically assumed threshold between incoherent and coherent emitters), and therefore must originate from a coherent emission process (M. P. Snelders et al. 2023). This makes them detectable across cosmic distances despite their relatively modest energetics compared to other extreme astrophysical phenomena.

The distribution of observed FRB spectral energies ($E_\nu$) follow a differential power law, where the rate above some spectral energy scales as $R\,(>E_\nu) \propto E_\nu^{\gamma_{\rm D}}$ for a differential index $\gamma_{\rm D}$. For the overall population of apparently non-repeating sources (C. W. James et al. 2022b; K. Shin et al. 2023), $\gamma_{\rm D} \sim -1.5$. Highly active repeating FRBs provide the opportunity to measure the burst energy distribution of a single source. In the case of repeaters, the energy distribution has been shown to deviate from a simple power law (D. Li et al. 2021; F. Kirsten et al. 2024).

The most energetic FRBs are also by far the most rare. Therefore, large on-sky time is essential to probe the extremes of the FRB population. By probing the maximum energetics of FRBs, we can constrain the emission mechanism (W. Lu, P. Kumar & R. Narayan 2019; A. J. Cooper & R. A. M. J. Wijers 2021); the total cosmic population (R. Luo et al. 2020; C. W. James et al. 2022b; K. Shin et al. 2023); and inform how best to detect FRBs with upcoming telescopes.

There are various conceivable ways to investigate the maximum achievable energies and luminosities of FRBs, including (1) discovery of exceptionally distant or energetic one-off bursts (S. D. Ryder et al. 2023); (2) population modelling of the full observed sample of FRBs (C. W. James et al. 2022b; K. Shin et al. 2023); and (3) high-cadence monitoring of hyperactive repeating sources (F. Kirsten et al. 2024; S. Z. Sheikh et al. 2024) (those repeaters that are sometimes seen to produce hundreds of bursts per hour, if observed with a high-sensitivity radio telescope). These methods complement each other, given that they are all subject to different observational biases and challenges. Moreover, it remains unclear whether apparently one-off and repeating FRBs share the same progenitors and emission mechanisms. By 'progenitor', we mean the type of astrophysical source powering the bursts, and by 'emission mechanism' we mean the physical process that generates the bursts. Probing the maximum observed energies of repeaters and apparently one-off FRBs is thus also a way to compare their nature.

In this work, we investigate the maximum burst energy and luminosity of FRB 20220912A, using multiple 25–32 m – class radio telescopes that together provide unprecedented observational coverage in terms of on-sky time. FRB 20220912A was discovered using the CHIME/FRB system (R. Mckinven & CHIME/FRB Collaboration 2022), and was soon identified as a hyperactive source compared to most other known repeaters. It was localized to a host galaxy at $z = 0.0771$ (V. Ravi et al. 2023; D. M. Hewitt et al. 2024) and has been the target of many follow-up observations. The exceptionally high activity of FRB 20220912A makes it an ideal source to map the burst energy distribution of a repeater. Here, we specifically focus on the maximum achievable burst energy and luminosity.

## 2 OBSERVATIONS

We observed FRB 20220912A using four European radio telescopes: the Westerbork RT-1 25-m in the Netherlands (Wb); the Onsala 25-m in Sweden (O8); the Stockert 25-m in Germany (St); and the Toruń 32-m in Poland (Tr). These observations span 117 d between MJD 59 867 and 59 983 (2022 October 15 until 2023 February 08) for a total of 2192 h, which reduces to 1491 hours of unique on-source time when taking into account the overlap between different observing modes and telescopes. During our campaign we observed at $P$ band (330 MHz), $L$ band (1.4 GHz), and $C$ band (4.7 GHz) with the aim of observing simultaneously over a wide bandwidth, as much as possible. Table 1 gives an overview of the different observing set-ups while Fig. B1 visually represents the observations that were taken. Our data recording and burst searching strategy match that of earlier work (F. Kirsten et al. 2024). At Wb, Tr, and O8 we recorded amplitude and phase data (raw voltages) and at St we recorded total



Downloaded from academic.oup.com/mnras/article/545/2/staf1937/8317171 by Universiteit van Amsterdam user on 09 October 2026

intensity data. We searched for bursts using standard methods adapted to the specifics of each telescope.

### 2.1 Westerbork, Onsala, and Toruń

The data reduction and burst search analysis at Westerbork, Onsala, and Toruń follows our custom pipeline, which has been previously described (F. Kirsten et al. 2024). At these three telescopes, we captured and stored the raw voltages (waveform data) in `.VDIF` format (A. Whitney et al. 2010), with dual circular polarizations and 2-bit sampling. In order to search for bursts, we converted the `.VDIF` data to 8-bit total intensity (Stokes I) SIGPROC filterbank files using `digifil` (W. Straten & M. Bailes 2011). In order to limit dispersive smearing within a channel, we made filterbanks with different time and frequency resolutions for searches at different observing bands. For *C* band observations, we made filterbanks with 4 μs time bins and 250 kHz wide frequency channels. For *L* band observations at Toruń this was 8 μs time bins and 62.5 kHz channels and for Westerbork 64 μs time bins and 62.5 kHz channels; while for *P* band we used 512 μs time bins and 7.8125 kHz channels.

We used `Heimdall` to search for bursts in the filterbank files. In order to minimize the amount of false positive candidates we set a signal-to-noise (S/N) threshold of 7 and limit the dispersion measure (DM) search to within $\pm$ 50 pc cm$^{-3}$ of the reported value of $\mathrm{DM_{FRB}} = 220\,\mathrm{pc\,cm^{-3}}$ (R. Mckinven & CHIME/FRB Collaboration 2022). We mitigate radio frequency interference (RFI) by applying a static mask, which excises certain frequency channels known to contain RFI. The identified burst candidates are then classified using the machine learning classifier `FETCH` (D. Agarwal et al. 2020), where we make use of models A & H and set a detection threshold of 50 per cent. The burst candidates that have a reported probability of at least 50 per cent in one of the two models are then all manually inspected. As a fail-safe we also manually inspect all burst candidates that have a reported DM within 5 pc cm$^{-3}$ of the expected DM.

Using the radiometer equation, we calculate both the detection and completeness thresholds for the observations (J. M. Cordes & M. A. McLaughlin 2003). The detection threshold represents the minimal fluence that our telescopes are sensitive to, while the completeness threshold represents the minimal fluence where we expect to detect (almost) all bursts. For the detection threshold we assume a 7$\sigma$ detection with a canonical adopted FRB width of 1 ms. For the completeness threshold we assume a conservative 15$\sigma$ threshold and take a burst width of 3 ms since we know that bursts originating from FRB 20220912A have generically longer durations than one millisecond (D. C. Konijn et al. 2024). The various detection and completeness thresholds of the instruments, per observing band, are listed in Table 1.

### 2.2 Stockert

At Stockert we record 32-bit total intensity data using the Pulsar Fast Fourier Transform (PFFTS) backend (E. D. Barr et al. 2013). These data are stored in `PFFTS` format. Using the `filterbank` tool from the SIGPROCpackage, we create `filterbank` files that consist of 32-bit floats. The time- and frequency resolution of the filterbanks are 218.45 μs and 586 kHz, respectively. We then search for bursts using tools from the PRESTOpackage (S. Ransom 2011). The `rfifind` tool is used to mitigate RFI, `prepsubband` then dedisperses the data using a DM of $\mathrm{DM_{FRB}} = 220\,\mathrm{pc\,cm^{-3}}$, and finally we search for burst candidates using `single_pulse_search` with a S/N limit of 8. Reported burst candidates are then classified using `FETCH` Model A and a detection threshold of 50 per cent. All automatically classified burst candidates are then manually inspected. The detection and completeness threshold are listed in Table 1.

### 2.3 Observational pointing

Westerbork and Toruń pointed towards RA = $23^{\mathrm{h}}09^{\mathrm{m}}05\overset{\mathrm{s}}{.}6$ Dec = $+48^{\circ}42'00\overset{''}{.}0$ (J2000), as published in the discovery report by R. Mckinven & CHIME/FRB Collaboration (2022). Onsala pointed towards RA = $23^{\mathrm{h}}09^{\mathrm{m}}05\overset{\mathrm{s}}{.}49$ Dec = $+48^{\circ}42'25\overset{''}{.}6$ (J2000), the initial localization as reported by DSA-110 (V. Ravi 2022a). Stockert initially also pointed towards the CHIME localization, but changed this to the DSA-110 localization after 2022 December 21. Even though there was an erratum for the DSA-110 localization (V. Ravi 2022b), we did not change our pointing. Regardless, the offset between the pointing directions of the telescopes and the best-known position of FRB 20220912A is less than ∼30 arcsec in all cases (D. M. Hewitt et al. 2024). This pointing offset is still well within the full-width at half maximum primary beams at different wavelengths, which range from 0.1° (*C* band) to 2.3° (*P* band).

## 3 ANALYSIS AND RESULTS

We detected 130 bursts from FRB 20220912A. Of these, 114 unique bursts were detected at 1.4 GHz, including 16 bursts that were detected by multiple telescopes simultaneously. Remarkably, the highest energy bursts from FRB 20220912A contributed to $22.0^{+15.6}_{-10.3}$ per cent of the all-sky rate of FRBs at *L* band ($\mathcal{F} >$ 500 Jy ms). We also detected 16 unique bursts at 330 MHz, while no bursts were detected at 4.7 GHz. Although we sometimes had simultaneous coverage between all observing bands, see Fig. B1, we did not detect any burst at multiple frequency bands. Each burst is labeled with an ID, Bx, numbered in order of their arrival time, and followed by the telescope code to indicate which instrument detected the burst (e.g. B15-Tr). A subset of bursts, preferentially those with high S/N, is shown in Fig. 1; a complete overview of all dynamic spectra is provided in the Supplementary material.

### 3.1 Burst properties

To correct for the dispersive delay we used a single DM for all bursts detected at *L* band (1.4 GHz). The value we used is 219.375 pc cm$^{-3}$, which was determined by D. M. Hewitt et al. (2023) from analysis of the extremely bright and broad-band microshots in a burst that was co-detected by NRT (B2 in that paper) and Westerbork (B52-Wb here). While the DM of FRB 20220912A is known to vary (D. M. Hewitt et al. 2023), we find that such variations have a negligible effect on the inferred fluences and hence energetics of the bursts, which is the main focus of this paper. Hence, we do not attempt to derive an optimal DM for each burst, but see Section B1.

The burst properties we use in our analyses were determined using the filterbank files created with `digifil` and the SPC-algorithm, previously referred to as Method III. RFI was mitigated by manually masking affected frequency channels for all bursts using the tools `psrzap` and `pazi` from the DSPSR software package. Additionally, we also zapped the edges of the subbands because of the drop in sensitivity at these frequencies (see, e.g. B35-st and B15-tr in Fig. 1).

To measure the time and frequency extent of the bursts we follow our earlier work (F. Kirsten et al. 2024). We manually determined the start and stop times of each individual component of a burst. For these time ranges we calculate the 2D autocorrelation function in time and frequency. We then fit a 1D Gaussian to the spectra and time series and determine the width both in time and frequency. We

Downloaded from academic.oup.com/mnras/article/545/2/staf1937/8317171 by Universiteit van Amsterdam user on 09 October 2026

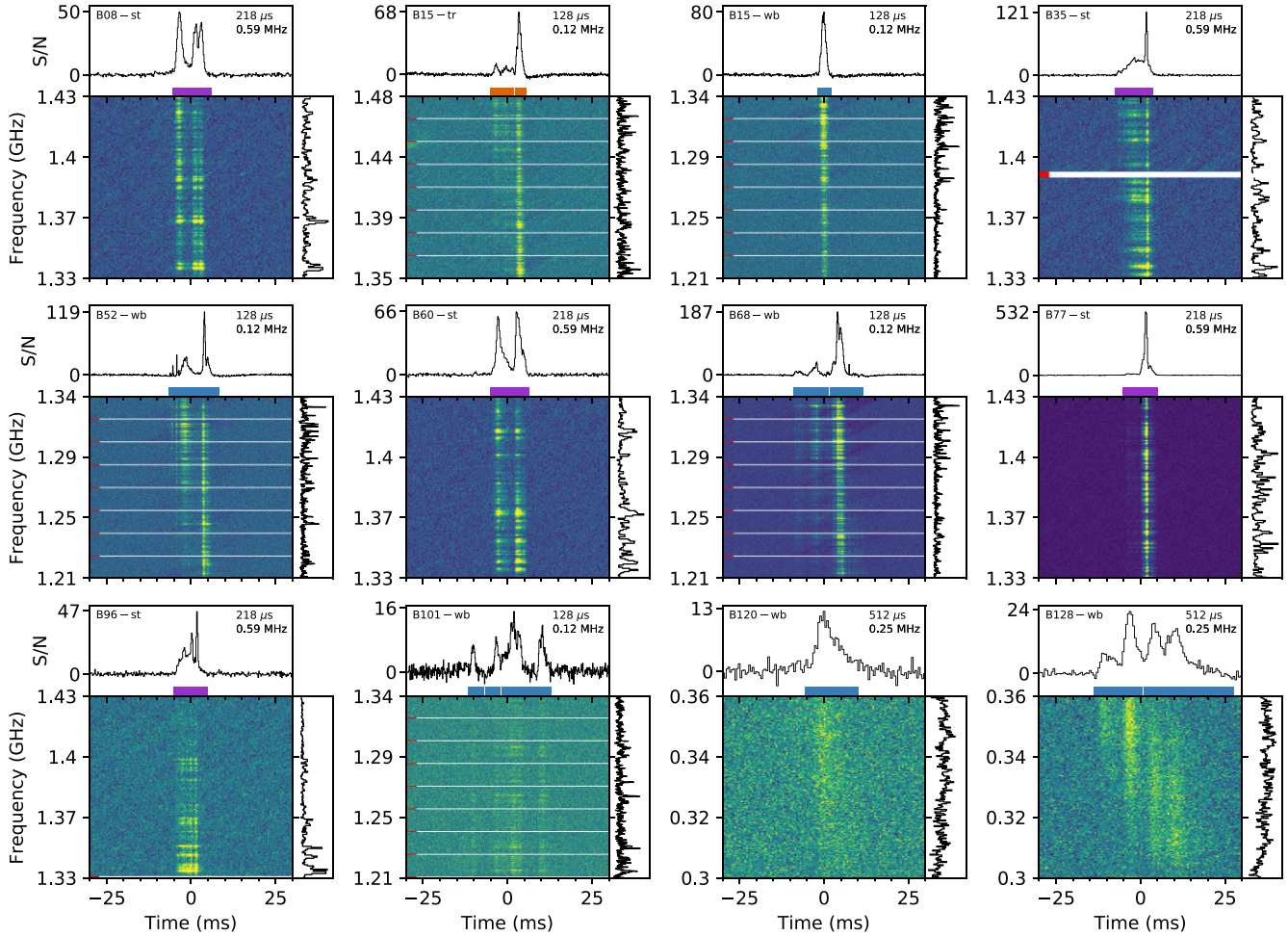


**Figure 1.** Dynamic spectra, time and temporal profiles for a subset of bursts. Each subfigure consists of three panels. Shown in the top panel is the burst-id, the time- and frequency resolution at which the data is plotted and the time profile of the burst. The horizontal bars represent the width for each component of a burst whereas the colour of the bars correspond the instrument used to detect the burst. Purple corresponds to Stockert (St), orange to Toruń (Tr), and blue to Westerbork (Wb). The side panel shows the temporal profile which is the sum over the time axis, but only under the horizontal bars. The white vertical lines are masked channels at the edges of the subbands or the presence of radio frequency interference (RFI) which are indicated by red ticks. The bursts have been corrected for dispersive effects where we used a value of 219.37 pc cm$^{-3}$ for bursts detected at 1.4 GHz (*L* band) and 219.73 pc cm$^{-3}$ for bursts detected at 0.3 GHz (*P* band). For Stockert this correction was applied incoherently (between frequency channels) and for Toruń and Westerbork this correction was applied incoherently and coherently (within frequency channels). The dynamic spectra of all detected bursts are available as part of the Supplementary material.

define the burst frequency extent to be the full extent of the observing frequency if the full width at half maximum (FWHM) of the Gaussian fit is more than 75 per cent of the total bandwidth. The fluence of a burst is determined using the radiometer equation and calculating the flux density per time bin while summing over the on-time region for each component (J. M. Cordes & M. A. McLaughlin 2003). An overview of burst properties can be found in Table 2.

Additionally, we also measured the fluences using filterbank files created by SFXC (Method I) and only `digifil` (Method II) in order to compare and quantify the digitization effects that are described in more detail in Section B2. The ratios of fluences between the three methods are shown in Fig. B3. We find that we encounter saturation effects that underestimate the fluences by up to 40 per cent (SFXC) and overestimate them by 10 per cent (`digifil`) for bursts detected at *L* band (left panel). For bursts detected at *P* band (right panel) the saturation effect is less apparent even though we detect bright bursts (>1000 Jy ms). This lack of saturation is most likely due to the longer dispersive sweep of the burst and the relatively low sensitivity of the Westerbork *P*-band receiver.

When determining the time of arrival (ToA) of a burst one has to take into account potential data loss during the recording of the `.VDIF` format data. `digifil` currently has no functionality to account for potential data loss that occurred during an observation. Instead, when creating a filterbank file, `digifil` will stitch together gaps in the data. In order to correct for this issue, we determined the ToAs of our detected bursts using SFXC. SFXC has the functionality to accurately handle data loss by padding the missing data with zero values. We create coherent dedispersed filterbank files for bursts observed with Wb and Tr at a time resolution of 64 μs for *L*-band bursts and 512 μs for *P*-band bursts. For St, missing data is padded in real time. Both programmes use the same assumed dispersive constant of $1/(2.41 \times 10^{-4})$ MHz$^2$ pc$^{-1}$ cm$^3$ s. We fit a Gaussian to every component in the time series for each burst. We define the ToA of a component as the centre of this fitted Gaussian and we set the ToA of a single burst as the centre of the Gaussian in case of a single component burst or the middle point between the left and right-most component in the case of a multicomponent burst. For the case of SFXC, the timestamps are reported with respect to the geocenter of



Downloaded from academic.oup.com/mnras/article/545/2/staf1937/8317171 by Universiteit van Amsterdam user on 09 October 2026

**Table 2.** Burst properties. The complete table and an additional table with properties per component for each burst can be found in the supplementary material.

| Burst ID[a] | Station | TOA[b] [MJD] | Peak S/N[c] | Fluence[d] [Jy ms] | Number of components | Width[e] [ms] | Spectral density[f] [$10^{29}$ erg Hz$^{-1}$] | Spectral luminosity[g] [$10^{32}$ erg s$^{-1}$ Hz$^{-1}$] | BW[h] [MHz] | Central frequency [MHz] |
|---|---|---|---|---|---|---|---|---|---|---|
| B01 | St | 59867.55026197426 | 14.90 | 42.16 ± 8.43 | 2 | 9.61 | 57.11 ± 11.42 | 5.94 ± 1.19 | 128 | 1381 |
| B02 | St | 59868.72071901775 | 8.91 | 24.26 ± 4.85 | 1 | 7.86 | 32.86 ± 6.57 | 4.18 ± 0.84 | 128 | 1381 |
| B03 | St | 59868.80699833712 | 4.69 | 29.73 ± 5.95 | 1 | 13.54 | 40.27 ± 8.05 | 2.97 ± 0.59 | 128 | 1381 |
| B04 | St | 59868.95206450199 | 4.41 | 11.8 ± 2.36 | 1 | 4.59 | 15.98 ± 3.2 | 3.48 ± 0.70 | 128 | 1381 |
| B05 | Tr | 59868.95206954337 | 16.67 | 40.75 ± 8.15 | 1 | 3.97 | 55.19 ± 11.04 | 13.91 ± 2.78 | 128 | 1414 |
| B06 | Tr | 59868.98521494057 | 5.89 | 20.31 ± 4.06 | 1 | 6.14 | 27.51 ± 5.5 | 4.48 ± 0.90 | 128 | 1414 |
| – | – | – | – | – | – | – | – | – | – | – |
| B127 | Wb | 59941.68738958076 | 6.99 | 274.25± 54.85 | 1 | 20.48 | 371.47 ± 74.29 | 18.14 ± 3.63 | 54 | 328 |
| B128 | Wb | 59941.73017555207 | 24.17 | 2629.4 ± 525.88 | 4 | 32.77 | 3561.49 ± 712.3 | 108.71 ± 21.74 | 54 | 328 |
| B129 | St | 59949.88269849737 | 6.78 | 46.15 ± 9.23 | 1 | 12.67 | 62.51 ± 12.5 | 4.93 ± 0.99 | 128 | 1381 |
| B131 | St | 59978.53235768391 | 39.33 | 375.07 ± 75.01 | 1 | 13.33 | 508.03 ± 101.61 | 38.13 ± 7.63 | 128 | 1381 |
| B132 | Tr | 59982.71918144583 | 22.65 | 50.59 ± 10.12 | 1 | 6.91 | 68.53 ± 13.71 | 9.92 ± 1.98 | 128 | 1414 |

[a]B84 was omitted due to it later being classified as radio frequency interference (RFI), B130 was removed because the presence of strong RFI made it impossible to measure its properties.
[b]Time of arrival referenced to the solar system barycenter at infinite frequency in TDB. We used a dispersion constant of 1/(2.41 × $10^{-4}$) MHz$^2$ pc$^{-1}$ cm$^3$ s. For detections with a central frequency of 328 MHz we used a DM of 219.735 pc cm$^{-3}$ and the others a DM of 219.37 pc cm$^{-3}$.
[c]The peak S/N of the brightest component.
[d]The sum of the computed fluences for each component measured after applying the SPC algorithm (method III). We assume a 20 per cent error for all bursts dominated by the uncertainty of the SEFD.
[e]The manually determined time span between the start of the first and end of the last component.
[f]Computed using equation (1), $D_L = 362.4$ Mpc and $z = 0.0771$.
[g]Spectral density divided by the width.
[h]The bandwidth of the burst used for the computation of the fluence.

the Earth with the reference frequency being the middle of the top subband. For `digifil`, the timestamps are local arrival times and the reference frequency is the middle of the top frequency channel. For both cases, we convert the arrival times to barycentric arrival times in the TDB time-scale with respect to infinite frequency for the assumed DM for *L* band and *P* band. An overview of all determined ToAs, per burst and per component, can be found in Table 2.

### 3.2 Detection and sky rate

We observed FRB 20220912A for 1158.57 and 607.34 unique hours at *L* and *P* band, respectively, and detected 13 and 7 bursts above a fluence $\mathcal{F} > 500$ Jy ms. This implies a detection rate of $0.27^{+0.19}_{-0.13}$ burst/day (*L* band) and $0.28^{+0.29}_{-0.17}$ burst/day (*P* band) for high-fluence bursts, where the errors are the 95 per cent Poisson uncertainty on the rates. Though the burst rates are consistent between the two bands, we caution that these multifrequency observations were not strictly simultaneous and both reflect an average rate over some range of time (Fig. B1).

Based on the ASKAP Fly Eye's survey (R. M. Shannon et al. 2018) and modelled number counts (W. Lu & A. L. Piro 2019) assuming a burst energy distribution with slope $\gamma_C = -1.5$, an all-sky rate at *L* band has been determined above a fluence $\mathcal{F} > 100$ Jy ms, $R_{sky}(\mathcal{F} > 100\ \text{Jy ms}) = 5 \times 10^3$ sky$^{-1}$ yr$^{-1}$. We detected 48 *L*-band bursts above 100 Jy ms, which corresponds to a rate of $7.3^{+2.4}_{-1.9}$ per cent $R_{sky}(\mathcal{F} > 100$ Jy ms) and agrees with the all-sky rate for the ATA sample of $5.8^{+3.4}_{-2.4}$ per cent (S. Z. Sheikh et al. 2024) (quoted errors are the 95 per cent Poisson uncertainty on the rates). For our brightest detections, 13 bursts above 500 Jy ms and four bursts above 1000 Jy ms, we find an all-sky rate of $22.0^{+15.6}_{-10.3}$ per cent $R_{sky}(\mathcal{F} > 500$ Jy ms) and $19.1^{+29.8}_{-13.9}$ per cent $R_{sky}(\mathcal{F} > 1000$ Jy ms), respectively. A similar calculation has been done for the all-sky rate contribution for FRB 20201124Awith a fluence larger than 500 Jy ms and was estimated to be $2.6^{+5.0}_{-2.0}$ per cent $R_{sky}(\mathcal{F} > 500$ Jy ms) (F. Kirsten et al. 2024). This illustrates that the contribution to the all-sky rate of FRB 20220912Awas almost an order of magnitude higher compared to FRB 20201124A for highly energetic bursts. Additionally, it underlines that a single hyperactive FRB repeater can strongly contribute to the all-sky rate for a relatively short time when the source is active. The upcoming, wide-field BURSTT (H.-H. Lin et al. 2022) telescope (FoV $\sim 10^4$ deg$^2$) should be an excellent system for identifying such sources.

### 3.3 Cumulative burst rates

In addition to the new data we present here, our analysis also makes use of three additional observational campaigns towards FRB 20220912A, which were performed during the same time range: 8.67 h of observations with the Five-hundred-metre Aperture Spherical Telescope (FAST; Y.-K. Zhang et al. 2023); 61 h of observations with the NançayRadio Telescope (NRT; D. C. Konijn et al. 2024); and 541 h of observations with the Allen Telescope Array (ATA; S. Z. Sheikh et al. 2024).

The cumulative burst distribution of FRBs is sometimes fit by a single power law $R\ (> E_\nu) \propto E_\nu^{\gamma_C}$, as has been done, e.g. for FRB 20121102A (K. Gourdji et al. 2019) and FRB 20200120E (K. Nimmo et al. 2023). Here $R$ is the rate of bursts, $E_\nu$ the spectral energy density of the bursts, and $\gamma_C$ is the slope of the cumulative distribution. To be able to compare distributions between telescopes, we express the energetics of the bursts as spectral energy density (erg Hz$^{-1}$), $E_\nu = E/\nu$. Where $\nu$ is the observed bandwidth of the burst. We convert the measured fluences to spectral energy via (J. P. Macquart & R. Ekers 2018),

$$E_\nu = \frac{\mathcal{F} \cdot 4\pi D_L^2}{(1+z)^{2+\alpha}}, \tag{1}$$

where $\mathcal{F}$ is the fluence of the burst, $4\pi D_L^2$ is the luminosity distance factor assuming isotropic emission, and $(1+z)^{2+\alpha}$ is the redshift correction, where $\alpha$ is the spectral index ($\mathcal{F}_\nu \propto \nu^\alpha$). We set $\alpha = 0$ to be consistent with respect to the fluence calculation. The fluence is calculated based on the band-averaged time series where we thus assume $\alpha = 0$. The luminosity distance ($D_L$) of FRB 20220912Ais



Downloaded from academic.oup.com/mnras/article/545/2/staf1937/8317171 by Universiteit van Amsterdam user on 09 October 2026

362.4 Mpc, with corresponding redshift $z = 0.0771$ (V. Ravi et al. 2022).

To fit a power law to the cumulative distribution, we exclude bursts that were detected below our completeness threshold for St, Wb, and Tr; see Table 1 for an overview of completeness thresholds per telescope and observing band. The sensitivity of NRT and FAST enables the detection of bursts of much lower spectral energy density ($E_{\rm min} \sim 10^{28}$–$10^{29}$ erg Hz$^{-1}$) where the cumulative distribution has been shown to deviate from a single power law (D. Li et al. 2021). In this work, we focus on a turnover towards the higher energies. Therefore, we use the PYTHON package POWERLAW (J. Alstott, E. Bullmore & D. Plenz 2014) to determine the minimum energy ($E_{\rm min}$) above which the distribution is best described by a power law. For FAST, we find $E_{\rm min}^{\rm FAST} = 5.6 \times 10^{29}$ erg Hz$^{-1}$ and for NRT we find $E_{\rm min}^{\rm nc} = 3.4 \times 10^{29}$ (erg Hz$^{-1}$).

An initial guess of the power law index is estimated using a maximum likelihood method (D. F. Crawford, D. L. Jauncey & H. S. Murdoch 1970; C. W. James et al. 2019). Next, we use `scipy.optimize.curvefit` to fit a power law, where we assume a fiducial uncertainty of 20 per cent on the energy of the burst. This uncertainty stems mainly from the uncertainty on the system equivalent flux density (SEFD) of each telescope. The error from `curvefit` is the first error we quote. In addition to the $1\sigma$ error quoted by `curvefit` we perform a bootstrapping method to estimate the variance of the fit. Bootstrapping is done by refitting the data with only a subset of the data points. We refitted the data 1000 times using 90 per cent of the data points without replacement. The error determined via bootstrapping is noted as the second error quoted on the derived values.

In Fig. 2, we show the cumulative burst energy distribution, denoted with slope $\gamma_{\rm C}$, for detections from Westerbork, Stockert, FAST, and NRT at $L$ band (1.4 GHz) – between MJD 59 869 (2022 October 17) and MJD 59 910 (2022 November 27). Constraining the time period allows us to directly compare the determined slopes for the different observational campaigns, while avoiding the potential pitfall of a burst energy distribution that evolves with time. For the high-energy bursts ($E_\nu > 3 \times 10^{30}$ erg Hz$^{-1}$) detected by Stockert we find a power-law index of $\gamma_{\rm C}^{\rm st} = -0.99 \pm 0.02 \pm 0.06$ and for Westerbork we find $\gamma_{\rm C}^{\rm Wb} = -0.74 \pm 0.05 \pm 0.08$. For the low-energy bursts ($E_\nu < 3 \times 10^{30}$ erg Hz$^{-1}$) from FAST we find a significantly steeper slope of $\gamma_{\rm C}^{\rm FAST} = -1.84 \pm 0.03 \pm 0.13$. Fig. 2 also shows the cumulative distribution for the bursts detected at $P$ band (330 MHz) by Westerbork, where we find a best-fitting power law with index $\gamma_{\rm C}^{\rm Wb} = -1.10 \pm 0.07 \pm 0.15$.

We find that the burst energy distribution of NRT is not well described by a single power law. This is apparent by eye, and by calculating the power-law slope using the maximum likelihood method as a function of the spectral energy density, as shown in the right panel of Fig. 3. We therefore fit a broken power law to the distribution and determine the breakpoint to be $E_{\rm break} \sim 3.2 \times 10^{30}$ erg Hz$^{-1}$. To be consistent in our methodology, we fit two separate power laws to the NRT data. For the first power law, for bursts that satisfy $E_{\rm min}^{\rm NRT} < E_\nu^{\rm NRT} < E_{\rm break}$, we find $\gamma_{\rm C}^{\rm NRT-1} = -1.69 \pm 0.01 \pm 0.05$. We fit a second power law for bursts that satisfy $E_{\rm break} < E_\nu^{\rm nc}$ and find $\gamma_{\rm C}^{\rm NRT-2} = -0.60 \pm 0.08 \pm 0.05$, as shown in the left panel of Fig. 3. Interestingly, the integrated total energy of the bursts in the low- and high-energy regimes of the energy distribution are roughly equal.

### 3.4 Turnover at the characteristic energy

As we expect a physical limit to FRB energies we investigate a possible turnover in the energy distribution. We combined detections from multiple observational studies constrained in time between MJD 59868 and MJD 59910. These studies were the NRT sample (D. C. Konijn et al. 2024), detections from ATA (S. Z. Sheikh et al. 2024) and FAST (Y.-K. Zhang et al. 2023), as well as the detections described in this work. We filtered out 5 duplicate bursts that were co-detected by the ATA and Stockert and only used the brightest detection in each case. We only consider bursts with energies larger than the completeness threshold of the least sensitive telescope (Westerbork at 24.4 Jy ms), see Table 1. We assume a Schechter function (P. Schechter 1976) as,

$$P(E_\nu) = N \left(\frac{E_\nu}{E_{\rm char}}\right)^{\gamma_{\rm D}} \exp\left[-\frac{E_\nu}{E_{\rm char}}\right], \quad (2)$$

where $E_\nu$ is the spectral energy density (erg Hz$^{-1}$), $\gamma_{\rm D}$ is the slope on the differential distribution, $E_{\rm char}$ is the cut-off energy, and $N$ is a normalization factor. We apply a Markov Chain Monte Carlo (MCMC) fitting technique to test if the combined burst sample is well described by a Schechter function. We bin the sample of bursts into 20 independent bins, and infer the model parameters using a Bayesian model comprised of a Poisson likelihood function appropriate for binned count data, and flat priors on the parameters. We set the flat prior on $E_{\rm char}$ to lie between 0 and 1000 in units of $10^{32}$ erg Hz$^{-1}$. We sampled the model using MCMC as implemented in EMCEE (D. Foreman-Mackey et al. 2013) with 100 walkers and 10 000 steps after 500 burn-in steps. A corner plot of the posterior probability densities generated with the CORNER package (D. Foreman-Mackey 2016) is shown in the left panel of Fig. 4. Tests using narrower priors on $E_{\rm char}$ between 0.5 and 50 in units of $10^{32}$ erg Hz$^{-1}$ produced similar results, indicating robustness against changes in prior density.

We find a characteristic maximum energy of $E_\nu^{\rm char} = 2.09^{+3.78}_{-1.04} \times 10^{32}$ (erg Hz$^{-1}$) with a differential power law index of $\gamma_{\rm D} = -1.12^{+0.17}_{-0.13}$ that we directly compare to previous modelling of one-off FRBs in Table 3. In Fig. 4, we show the differential distribution of burst energies over-plotted with a Schechter function using the median values of the posterior distributions from the MCMC run. We also indicate the determined characteristic maximum energy and uncertainty range.

## 4 DISCUSSION

### 4.1 Activity of hyperactive repeaters

We find that the burst energy distribution of FRB 20220912A cannot be described by a single power law. Rather, it is well described by a broken power law ($E_\nu^{\rm break} \sim 3.2 \times 10^{30}$ erg Hz$^{-1}$) and an exponential cut-off ($E_\nu^{\rm char} = 2.09^{+3.78}_{-1.04} \times 10^{32}$ erg Hz$^{-1}$). The burst energy distribution is steeper ($\gamma_{\rm C}^{\rm NRT-1} = -1.69 \pm 0.01 \pm 0.05$) below the break, and flatter ($\gamma_{\rm C}^{\rm NRT-2} = -0.60 \pm 0.08 \pm 0.05$) above it. Previous work also showed that another hyperactive repeater, FRB 20201124A, has a similar break in its energy distribution at ($E_\nu^{\rm break} \sim 8 \times 10^{30}$ erg Hz$^{-1}$) as well as a similar flattening: from $\gamma_{\rm C}^{\rm FAST} = -1.95 \pm 0.001 \pm 0.06$ at lower energies to $\gamma_{\rm C}^{\rm O8+St} = -0.48 \pm 0.11 \pm 0.03$ at the highest burst energies (F. Kirsten et al. 2024). The occurrence of a break requires explanation; it could indicate two populations of bursts produced by distinct physical mechanisms (F. Kirsten et al. 2024). Approximately a similar amount of total energy is released by the source above and below the break. The similarity in the break point energy between FRB 20220912Aand FRB 20201124A suggests that this is a common feature that may be observed in the future for other repeaters.

For FRB 20201124A, mapping the energy distribution required comparing high-energy bursts from high-cadence observations with



Downloaded from academic.oup.com/mnras/article/545/2/staf1937/8317171 by Universiteit van Amsterdam user on 09 October 2026

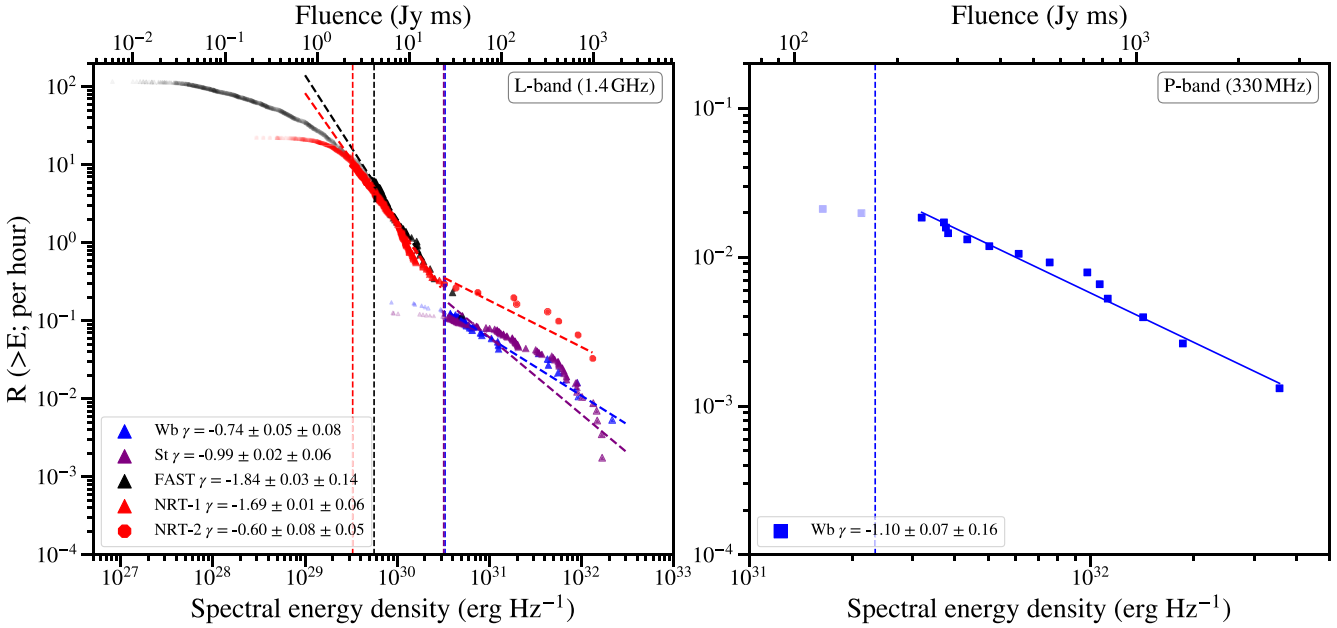


**Figure 2.** Cumulative burst energy distribution of spectral energy densities. In the left panel, we show detections by Westerbork (Wb) and Stockert (St), FAST (Y.-K. Zhang et al. 2023), and NRT (D. C. Konijn et al. 2024) at 1.4 GHz (*L* band). In order compare between the different observational campaigns we only show bursts that were observed between MJD 59869 and 59910. Comparing the different rates reveals a break in the distribution towards higher energies ($\sim 3 \times 10^{30}$ erg Hz$^{-1}$). The purple and blue vertical line correspond to the completeness threshold as indicated in Table 1. The red and black vertical lines denote the point where the distribution can be best described by a single power law as calculated by the PYTHON package POWERLAW. Transparent data points which are on the left side of the vertical lines were excluded in the fit. When fitting we set a 20 per cent error on the energies and quote two errors. The first error is the $1\sigma$ statistical uncertainty on the fit and the second error is the $1\sigma$ error after the bootstrapping method. In the right panel, we show detections observed at 0.3 GHz (*P* band).

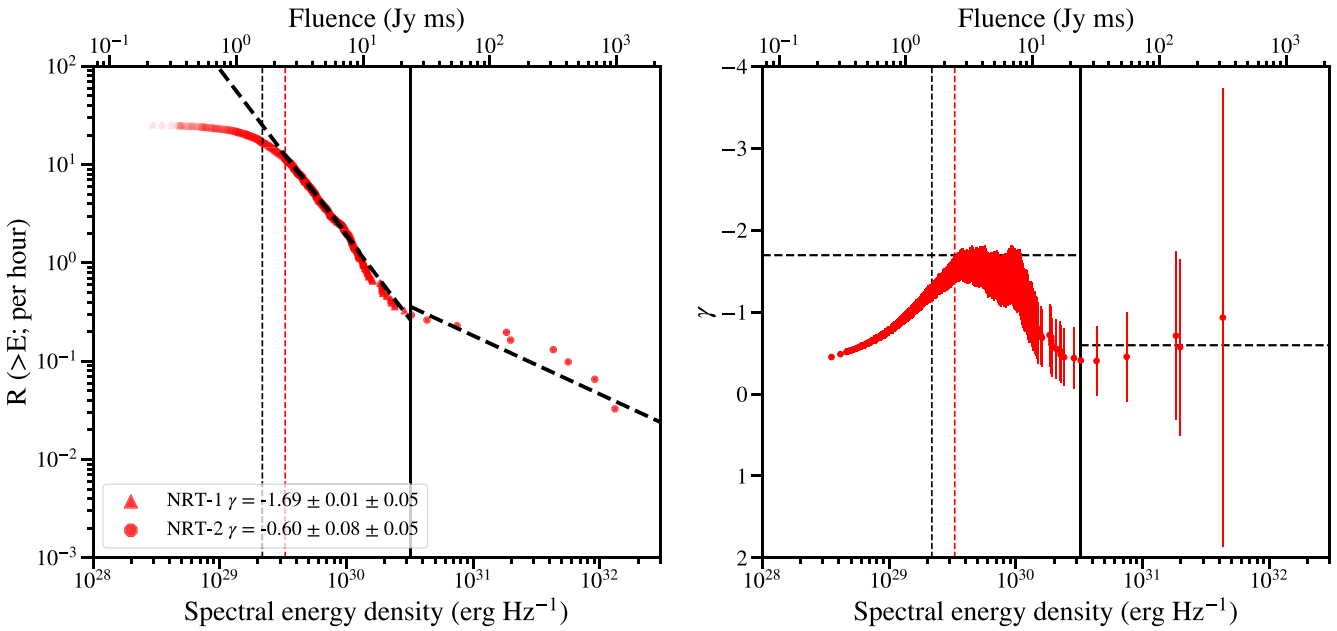


**Figure 3.** Cumulative burst energy distribution for bursts detected by NRT. Left: The cumulative energy distribution for NRT, also shown in Fig. 2, fitted with two power laws. The vertical dotted black line is the estimated completeness threshold and the vertical dotted red line indicates the turnover point as estimated using the POWERLAW package. The solid black line corresponds to the determined breakpoint of the distribution at $E_{\rm break} = 3.2 \times 10^{30}$ erg Hz$^{-1}$. Right: the power law index ($\gamma_{\rm C}$) as a function of the spectral energy density calculated by a maximum-likelihood estimation. The horizontal dotted lines indicate the slopes of the power law used in the left panel.

Downloaded from academic.oup.com/mnras/article/545/2/staf1937/8317171 by Universiteit van Amsterdam user on 09 October 2026

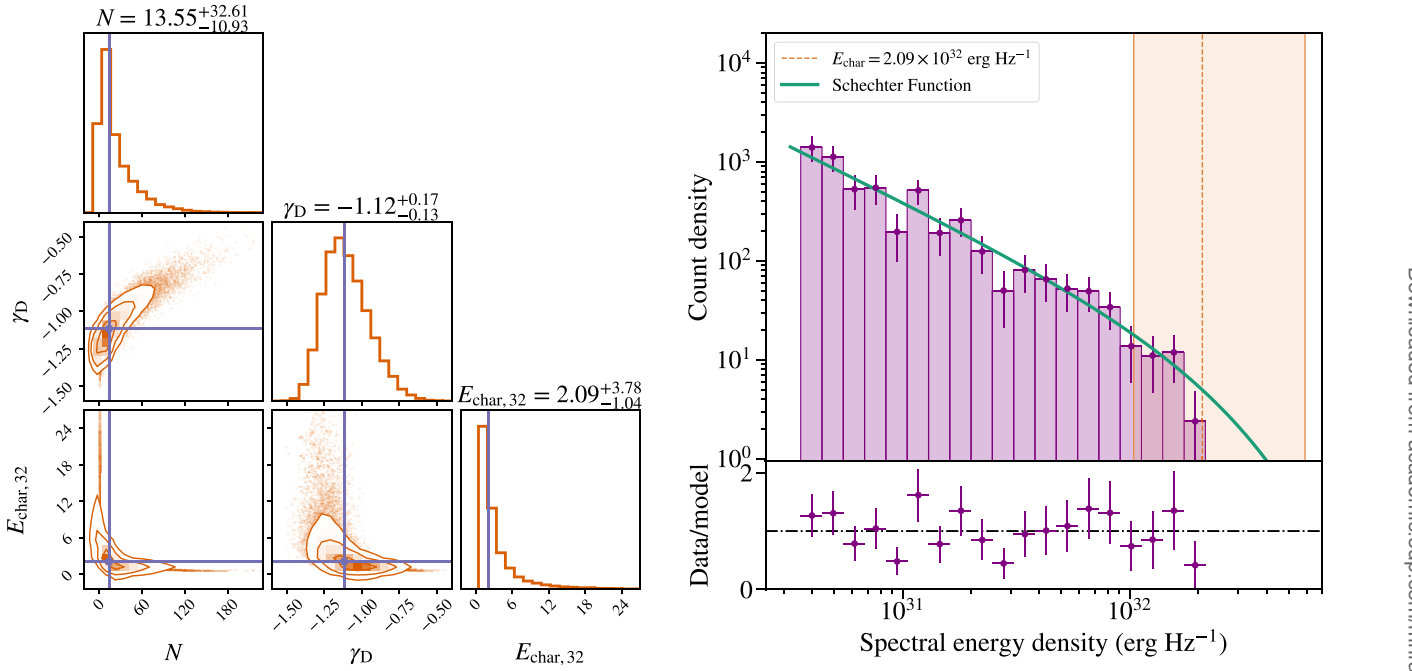


**Figure 4. Spectral energy densities modelled by a Schechter function.** Left: corner plot of the results from the MCMC analysis, thinned by a factor 30 for visual purposes. The solid lines denote the median values of the posterior distributions and the errors are the 16 per cent and 84 per cent quantile. Right: The differential distribution in the top panel includes bursts above 3.3 $\times$ $10^{30}$ erg Hz$^{-1}$ (or 24.4 Jy ms) detected by Westerbork, Stockert, Toruń, NRT, ATA, and FAST between MJD 59 869 and 59910. The line is an over-plotted Schechter function based on the median values of the posterior distribution of the MCMC analysis. The vertical dashed line is the best-fitting value for the characteristic energy with the region corresponding to error region of the 16 per cent and 84 per cent quantile. The bottom panel shows the ratio between the data and the Schechter model.

**Table 3.** Best Schechter fit results from different studies.

| | $\log_{10} E^{\rm char}$ [erg][a] | $\gamma_D$[b] | $\mathcal{F}_{\rm min}$[Jy ms][e] |
|---|---|---|---|
| This work | $41.32^{+0.45}_{-0.30}$ | $-1.12^{+0.17}_{-0.13}$ | 24.4 |
| S. D. Ryder et al. (2023)[c] | $41.7^{+0.2}_{-0.2}$ | – | – |
| K. Shin et al. (2023) | $41.38^{+0.51}_{-0.50}$ | $-1.30^{+0.7}_{-0.4}$ | 5.0 |
| C. W. James et al. (2022b) | $41.26^{+0.27}_{-0.22}$ | $-1.95^{+0.18}_{-0.15}$ | 0.5/4.4/21.9[f] |
| R. Luo et al. (2020)[d] | $42.08^{+0.30}_{-0.06}$ | $-1.79^{+0.31}_{-0.35}$ | 0.55 |

[a]Energy assuming a canonical adopted bandwidth of 1 GHz.
[b]Best fitted slope parameters on a differential distribution.
[c]Based on the sample of C. W. James et al. (2022b).
[d]Luminosity ($L_*$) converted using the average width from Table 2 of $\bar{w}$ = 4.14 ms.
[e]Fluence limits on the different observational campaigns.
[f]From C. W. James et al. (2022a).

25–32 m-class telescopes (F. Kirsten et al. 2024) with lower energy burst detections from FAST (H. Xu et al. 2022). For FRB 20220912A we follow the same approach, comparing our detections to the lower energy bursts observed by FAST (Y.-K. Zhang et al. 2023). Additionally, we are able to detect the break in the power law burst energy distribution using NRT data alone (D. C. Konijn et al. 2024) because NRT has good sensitivity and ample exposure time during the most intense period of activity (Figs 2 and 3; in comparison, the smaller dishes have a lower apparent rate because they missed the highest activity window around MJD 59879). The NRT distribution initially follows the slope of FAST, but then breaks and flattens towards higher energies following the slope of St and Wb. The observation of a break in the distribution by a single instrument is unprecedented; it underlines and confirms the flattening of the energy distribution towards higher energies.

The ATA observed FRB 20220912Afor 541 h and fit a power law to the cumulative distribution of burst energies (S. Z. Sheikh et al. 2024). They find a slope of $\gamma_C^{\rm ATA} = -1.08^{+0.25}_{-0.25}$. The energy range we are able to probe in this work overlaps with the ATA and allows for direct comparison. We find that the slopes for different instruments beyond the break point in the distribution, see Fig. 2, are consistent within uncertainties between all telescopes.

The telescopes used in this work (St, Wb, Tr, and O8) all have observing bandwidths ranging between 56–256 MHz, which is considerably narrower compared with the ATA (672 MHz) and NRT (512 MHz). Comparing the results of the cumulative power-law indices between all telescopes in the high-energy range shows comparable results, which indicates that the flattening in the distribution towards higher energies cannot simply be accounted for by the limited bandwidth of observation.

We observed 14 bursts at $P$ band above our completion threshold, see Fig. 2. Based on our sample we are unable to shed light on whether the cumulative energy distribution breaks at the same energy compared to $L$ band and if the differential distribution turns over at a similar characteristic energy. To further investigate the presence of a break-point at low radio frequencies, requires a higher sensitivity observational campaign capable of probing bursts in the lower energy regime ($E_\nu < 10^{30}$ erg Hz$^{-1}$).

### 4.2 Characteristic maximum energy

Determining the characteristic maximum spectral energies of FRBs is crucial to constrain their emission mechanisms and nature. For FRB 20220912A we find $E_\nu^{\rm char} = 2.09^{+3.78}_{-1.04} \times 10^{32}$ erg Hz$^{-1}$ or,



Downloaded from academic.oup.com/mnras/article/545/2/staf1937/8317171 by Universiteit van Amsterdam user on 09 October 2026

equivalently, a total energy $\log_{10}(E^{\rm char}) = 41.32^{+0.45}_{-0.30}$ erg, assuming a 1-GHz emission bandwidth (Fig. 4). Our findings agree with the inferred fluence limit $\mathcal{F} \lesssim 10^4$ Jy ms (S. Z. Sheikh et al. 2024) (or, equivalently, $\log_{10}(E^{\rm char}) = 42.15$ erg) for FRB 20220912A to be consistent with the all-sky fluence distribution extrapolated from ASKAP Fly's Eye survey (R. M. Shannon et al. 2018).

Previously, constraints on $E^{\rm char}$ have been derived from population studies of apparently one-off FRBs. In these cases, the energy distribution is modelled as a Schechter function. Two of these studies combined data from various surveys including UTMOST, HTRU, and CRAFT (R. Luo et al. 2020), with another study only using the FRBs in the first CHIME/FRB catalogue (K. Shin et al. 2023). The detection of an FRB at $z = 1.016$ with an implied burst energy of $6.4 \pm 0.7 \times 10^{41}$ erg also enabled a strong constraint on the characteristic maximum energy (C. W. James et al. 2022b). From these various studies, $E^{\rm char}$ ranges between $\log_{10}(E^{\rm char}) = 41.26$–$42.08$ erg (Table 3). Our determined value of $E^{\rm char}$ for FRB 20220912A is consistent with the different population studies of apparently one-off FRBs.

However, in this comparison we have assumed a fiducial 1 GHz emission bandwidth for both repeaters and (apparent) non-repeaters alike. While the broad-band spectra of FRBs are still poorly constrained in general, previous studies with CHIME/FRB have found a systematic difference in the emission bandwidths of repeaters versus (apparent) non-repeaters Z. Pleunis et al. (2021). Given this, our $\log_{10}(E^{\rm char})$ value could be a factor of 2–3× lower if FRB 20220912A bursts are restricted to 300–500 MHz emission bandwidths. While previous studies have found restricted emission bandwidth for FRB 20220912A (D. C. Konijn et al. 2024; S. Z. Sheikh et al. 2024) in the ∼1–2 GHz range, its instantaneous emission bandwidth across the entire radio frequency range is unknown. Thus, for simplicity, and given the lack of a better model, we scale our total energies to a common 1-GHz emission bandwidth for both repeaters and (apparent) non-repeaters.

For the slope of the differential distribution, we find $\gamma_{\rm D} = -1.12^{+0.17}_{-0.13}$, which agrees with previous studies though the uncertainties on the measured slopes are large (Table 3). In our fitting of a Schechter function, we have only considered bursts above the completeness threshold of the least sensitive telescope (Wb) and with $E_\nu^{\rm char} > 3.3 \times 10^{30}$ erg Hz$^{-1}$, to avoid bursts that follow a steeper power-law index below this value (Fig. 2). We note that previous population studies may be including low-energy bursts that follow a different energy distribution, and which would skew the power-law slope of a Schechter fit to be apparently steeper.

During our burst search, we set the detection threshold at S/N > 7. However, in our previous work (F. Kirsten et al. 2024), we adopted a conservative approach and assumed a S/N of 15 as our completeness threshold. In this work, we test the dependence of the characteristic maximum energy on the adopted completeness threshold by varying the assumed S/N. Varying the threshold involves modelling of the Schechter function with different total number of bursts, see Supplementary Table 4. The completeness thresholds are referenced with respect to the completeness of the least sensitive telescope (Wb). For a threshold of $10\sigma$, the reduced chi-square implies a poor fit, which can be explained by our sample of detections from the 25–32-m telescopes being incomplete at that threshold. Adopting higher detection thresholds of 20− and $30\sigma$ results in $\chi^2 < 1$, which indicates overfitting of the data. Placing the completeness threshold exactly at the breakpoint ($E_{\rm break}$) of the distribution gave results consistent with those for a $15\sigma$ threshold, suggesting that this threshold appropriately characterizes our observations. We fit the Schechter function to the burst energy distribution, which was grouped into 20 independent bins. Running the same analysis with 15 and 25 bins produced consistent results, demonstrating that the fits do not strongly depend on the chosen binning.

To test whether a Schechter function is preferred over a simpler power-law function, we performed an identical MCMC analysis for a power-law model. This allowed us to compute the Bayesian information criterion (BIC), which is defined as:

$$\mathrm{BIC} = \mathrm{k}\ln(\mathrm{n}) - 2\ln(\hat{\mathrm{L}}), \tag{3}$$

where $k$ is the number of parameters, $n$ the number of data points and $\hat{L}$ is the sample with the highest likelihood from an MCMC chain. The number of data points is in both models taken as the number of bins ($n = 20$); the number of parameters is $k = 2$ for the power-law function and $k = 3$ for the Schechter function. Since we make use of flat priors, we take the sample with the highest probability as the maximum likelihood sample, which is $\ln(\hat{L}) = -41.64$ for the power-law function and $\ln(\hat{L}) = -33.53$ for the Schechter function. This results in BIC values of 89.26 for the power-law function and 76.05 for the Schechter function. A BIC difference of 13.21 indicates that the fitting of the Schechter function is a more appropriate description of the data. This is because the burst energies abruptly cut off around $2 \times 10^{32}$ erg Hz$^{-1}$, even though our observations could have detected bursts above this threshold.

### 4.3 Comparison to energy distributions of pulsars

Pulsars produce microsecond-to-millisecond duration coherent radio pulses, which are observationally similar to FRBs; they are hence a useful point of reference, even if the energy scales and progenitors of FRBs are different in nature. Some pulsars emit giant pulses (GPs) which show a burst distribution that could be described with a break and flattening toward higher energies. For PSR B1937+21 a break occurs in the cumulative distribution for pulses with a pulse energy larger than 7 Jy μs (J. W. McKee et al. 2019). These results were not found in previous studies on this pulsar (I. Cognard et al. 1996; V. A. Soglasnov et al. 2004), which could be due to the much shorter exposure times. the cumulative distribution of PSR B0540−69 does show a flattening in the distribution for higher energetic bursts (M. Geyer et al. 2021). Another well-studied emitter of GPs is PSR B0531+21 (the Crab Pulsar). The term 'supergiant pulse' was coined for pulses that show inconsistency with the probability implied by a simple power law (J. M. Cordes et al. 2004). These findings of a flattening were confirmed after 100 h of observing with the Green Bank telescope (M. B. Mickaliger et al. 2012). A more recent study did not find any hint of flattening in the distribution of supergiant pulses ($\mathcal{F} > 130$ Jy ms) after observing the Crab pulsar for 260 h (A. Bera & J. N. Chengalur 2019). Although we see similarities between FRBs and pulsars in their cumulative energy distributions, their energies differ by at least four orders of magnitude. A shared rotationally powered emission mechanism between pulsars and FRBs is ruled out; it is more likely that FRBs are magnetically powered (M. Lyutikov 2017). To our knowledge, systematic flattening of pulsar energy distributions at high energies has not been studied in detail for a population of sources.

### 4.4 Constraining the FRB emission mechanism

Extremely bright FRBs are valuable for constraining the progenitors and emission mechanisms of FRBs. To examine these constraints, we consider the most energetic bursts observed at $L$ band and $P$ band: B68-Wb and B128-Wb, respectively. These bursts have

Downloaded from academic.oup.com/mnras/article/545/2/staf1937/8317171 by Universiteit van Amsterdam user on 09 October 2026

**Table 4.** Schechter function parameter results. Results and best-fitting parameters from the MCMC analysis on fitting a Schechter function to the differential burst distribution by varying the fluence/energy threshold for bursts detected between MJD 59869 and 59910. The top row denotes the the completeness threshold and parameter values which were used in Fig. 4.

| $\sigma$ Threshold | Fluence threshold [Jy ms] | Spectral energy threshold [$10^{30}$ erg Hz$^{-1}$] | Total bursts | $N_{\rm Wb}$ | $N_{\rm St}$ | $N_{\rm Tr}$ | $N_{\rm ATA}$ | $N_{\rm Nc}$ | $N_{\rm Fast}$ | $N$ | $\gamma_{\rm D}$ | $E^{\rm char}$ [$10^{32}$ erg Hz$^{-1}$] | $\chi^2_\nu$ |
|---|---|---|---|---|---|---|---|---|---|---|---|---|---|
| 15[b] | 24.40 | 3.30 | 125 | 22 | 62 | 2 | 8 | 29 | 2 | $13.55^{+32.61}_{-10.93}$ | $-1.12^{+0.17}_{-0.13}$ | $2.09^{+3.78}_{-1.04}$ | 0.78 |
| 10 | 16.10 | 2.18 | 146 | 25 | 68 | 4 | 13 | 32 | 4 | $9.68^{+24.87}_{-8.30}$ | $-1.14^{+0.14}_{-0.10}$ | $2.54^{+6.87}_{-1.33}$ | 1.13 |
| 14.55[a] | 23.81 | 3.22 | 130 | 23 | 64 | 2 | 9 | 30 | 2 | $12.44^{+28.52}_{-10.14}$ | $-1.13^{+0.16}_{-0.12}$ | $2.16^{+4.22}_{-1.06}$ | 0.85 |
| 20 | 32.45 | 4.40 | 112 | 20 | 55 | 2 | 7 | 27 | 1 | $20.32^{+40.40}_{-16.08}$ | $-1.05^{+0.20}_{-0.15}$ | $1.68^{+2.70}_{-0.76}$ | 0.66 |
| 30 | 48.80 | 6.61 | 93 | 12 | 47 | 1 | 7 | 26 | 0 | $40.06^{+66.02}_{-31.28}$ | $-0.90^{+0.28}_{-0.23}$ | $1.19^{+1.68}_{-0.49}$ | 0.50 |

[a]Energy threshold corresponding the the break-point of the power law determined for NRT, see Fig. 3.
[b]The completion threshold corresponding to the least sensitive telescope (Wb). The result of this fit are shown in Fig. 4.

measured energies of $2.8 \times 10^{40}$ and $2.0 \times 10^{40}$ erg, respectively, determined by multiplying the observed spectral energy density with the bandwidth of each burst. To be more conservative, this calculation differs from previous calculations where we use a canonical adopted bandwidth of 1 GHz to convert to burst energies. As such, these values can be considered as lower limits on the isotropic-equivalent burst energy.

For typical radio efficiencies assumed in 'far-away' FRB models (B. D. Metzger et al. 2019) of $\epsilon_{\rm radio} \approx 10^{-5}$, these bursts require extreme event energies $E_{\rm flare} > 10^{45}$ erg, consistent with magnetar giant flares. Magnetospheric 'close-in' FRB models often invoke crustal dislocations as the mechanism by which particle acceleration is triggered. Given an event energy, a required magnetic field can be derived assuming fiducial crustal oscillation parameters (Z. Wadiasingh et al. 2020). If $\epsilon_{\rm radio} \approx 10^{-5}$, an FRB with $E_{\rm FRB} = 2 \times 10^{40}$ erg implies a local field strength $B \approx 2 \times 10^{16}$ G, suggesting that B68-Wb/B128-Wb require very large magnetic fields, plausibly stemming from multipolar field components or extreme crustal dislocations. We note that this magnetic field requirement corresponds to the specific mechanism presented in Z. Wadiasingh et al. (2020).

Coherent curvature radiation (CCR) by bunches has been discussed as a radiation mechanism for generating magnetospheric FRBs (P. Kumar, W. Lu & M. Bhattacharya 2017; W.-Y. Wang, R. Xu & X. Chen 2020). There is a maximum peak luminosity of CCR based on a upper limit to the electric field $E_\parallel$, above which Schwinger pairs rapidly screen the field (W. Lu & P. Kumar 2019; see also P. Kumar & Ž. Bošnjak 2020). The requirement that the momenta of radiating particles remains well-aligned also implies a maximal bunch luminosity (A. J. Cooper & R. A. M. J. Wijers 2021).

To characterize the limit of these constraints on the source of FRB 20220912A, we consider the burst in our sample with the highest peak luminosity ($S_\nu$): B77-St. We calculate the luminosity as (J. P. Macquart & R. Ekers 2018),

$$L_\nu = \frac{S_\nu \cdot 4\pi D_{\rm L}^2}{(1+z)^{1+\alpha}}, \tag{4}$$

where $S_\nu$ is the peak flux density, $4\pi D_{\rm L}^2$ the distance luminosity factor and $(1+z)^{1+\alpha}$ the redshift correction. resulting in a peak spectral luminosity of $L_{\nu,\rm B77-st} = 1.38 \times 10^{35}$ erg s$^{-1}$ Hz$^{-1}$, measured at a time resolution of $\Delta t = 218.45\,\mu$s. In Fig. 5, we show the minimum local magnetic field of the emission region based on the aforementioned maximum luminosities. These limits set conservative constraints on the surface magnetic field (e.g. corresponding to emission directly from the surface). Therefore, if B77-St is powered by CCR along open field lines, it must stem from a region with $B \gtrsim 10^{12}$ G.

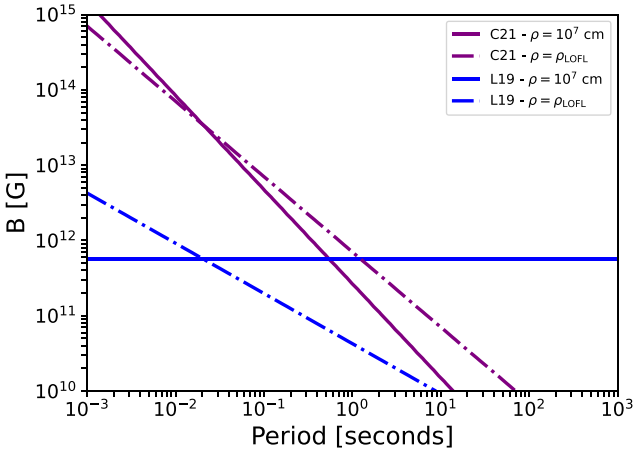


**Figure 5.** Magnetic field constraints for B77-St. Minimum local magnetic field $B$ as a function of neutron period for B77-St assuming CCR (W. Lu & P. Kumar 2019; A. J. Cooper & R. A. M. J. Wijers 2021). Solid lines refer to fixed field line curvature radius of $\rho_{\rm c} = 10^7$ cm, dot-dashed lines refer to emission along the last open field line (LOFL) at the polar cap co-latitude.

### 4.5 Source energy reservoir constraints

Assuming a perfect dipolar magnetic field, the total external magnetospheric energy reservoir of a neutron star can be crudely estimated as:

$$U_{\rm B} \approx \frac{R_{\rm NS}^3 B_{\rm s}^2}{6} \approx 1.7 \times 10^{47}\,{\rm erg} \left(\frac{R_{\rm NS}}{10^6\,{\rm cm}}\right)^3 \left(\frac{B_{\rm s}}{10^{15}\,{\rm G}}\right)^2. \tag{5}$$

Here, $B_{\rm s}$ is the surface magnetic field and $R_{\rm NS}$ is the neutron star radius. To examine the total energetics we integrate over the best-fitting differential burst energy distribution function (Fig. 4). The total radio energy of bursts observed across the 1769 unique observing hours of all observing campaigns at $L$ band included in the data set (assuming minimal overlap) above $E_{\rm radio,min} = 3.3 \times 10^{30}$ erg Hz$^{-1}$ is: $1.3 \times 10^{42}$ erg or $7.5 \times 10^{38}$erg h$^{-1}$ (assuming a conservative emission bandwidth $\Delta\nu \approx 100$ MHz, given our limited observing bandwidth). If we naively assume that the luminosity beaming enhancement and radio bursts missed due to beaming cancel out, as well as a radio efficiency factor of $\epsilon_{\rm radio} = 10^{-5}$, we find the external magnetic energy will be depleted on a time-scale:

$$\tau \approx 2150\,{\rm h} \left(\frac{B_{\rm s}}{10^{15}{\rm G}}\right)^2 \left(\frac{\epsilon_{\rm radio}}{10^{-5}}\right). \tag{6}$$

From Fig. 2, we can see that a roughly equal amount of integrated energy is released $E_{\rm radio,min} < 3.3 \times 10^{30}$. This estimate is in good



Downloaded from academic.oup.com/mnras/article/545/2/staf1937/8317171 by Universiteit van Amsterdam user on 09 October 2026

agreement with the estimated integrated power of lower energy bursts observed by FAST (Y.-K. Zhang et al. 2023) if a similar $\epsilon_{\rm radio}$ is assumed, despite caveats to the approximation including the non-uniformity of the true burst rate and the unknown beam1ing characteristics. This result implies that if a magnetar powers FRB 20220912A, the radio efficiency may be $\epsilon_{\rm radio} > 10^{-5}$, the external magnetic field may be $B > 10^{15}$ G, the external magnetic field is continuously replenished (e.g. via core field expulsion), or strong multipolar field components power most of the emitted energy. These findings are in agreement with the conclusions of J.-S. Zhang et al. (2025), who find that the cumulative energy of over 11 000 bursts detected from FRB 20240114A nearly deplete the energy stored in the magnetic field of a typical magnetar.

### 4.6 Energetics and multiwavelength counterparts

Multiwavelength counterparts to FRBs are expected within both magnetospheric (A. J. Cooper & R. A. M. J. Wijers 2021; Y.-P. Yang & B. Zhang 2021) and particularly maser shock models (B. D. Metzger et al. 2019). Simultaneous X-ray counterparts, as observed for the FRB-like burst from SGR 1935+2154 (C. K. Li et al. 2021; A. Ridnaia et al. 2021; M. Tavani et al. 2021) and prompt optical afterglows from FRB-associated flares (M. Lyutikov & D. R. Lorimer 2016; C. D. Kilpatrick et al. 2021; A. J. Cooper et al. 2022) are the most likely detectable counterparts to extragalactic FRBs.

Constraints on high-energy counterparts have been placed A. B. Pearlman et al. (2025) for bursts from the closest repeating extragalactic FRB source: FRB 20200120E at just 3.6 Mpc (M. Bhardwaj et al. 2021). The most energetic FRB from this source ($E_{\rm r,B4} = 2.8 \times 10^{33}$ erg) was detected simultaneous to NICER observations, broadly ruling out any simultaneous giant or intermediate magnetar X-ray flares (A. B. Pearlman et al. 2025). The most energetic bursts presented in this work are roughly seven orders of magnitude larger in total radio energy, at a distance approximately 100 times greater meaning, for similar radio efficiencies, multiwavelength fluxes coincident with the brightest bursts presented here should be a factor $\sim 10^3$ times higher. This bolsters the case for sensitive X-ray observations of prolific repeaters known to produce very bright bursts, notwithstanding the challenging large required time on source.

In Fig. 6, we show the predicted approximate optical (680 nm) afterglow light curves of B68-Wb and B128-Wb following previous maser shock afterglow formulations (B. Margalit et al. 2020; A. J. Cooper et al. 2022). In lieu of an X-ray detection, we normalize the light curves assuming an unobserved, quasi-simultaneous X-ray counterpart a factor $L_{\rm X}/L_{\rm r}$ more luminous than the FRB. We also show $5\sigma$ upper limits obtained by the ATLAS telescope network (J. L. Tonry et al. 2018) the night following B68-Wb in the 'orange' 560–820 nm band, and include representative limiting magnitudes of the ARCTIC telescope (J. Huehnerhoff et al. 2016), which has previously been utilized to constrain optical FRB afterglows (C. D. Kilpatrick et al. 2021).

### 4.7 Prospects for detecting more high-energy FRBs

Following a method employed in earlier work (F. Kirsten et al. 2024), we can place a limit on the maximum observable redshift based on our brightest detections at both 1.4 and 330 MHz. Our brightest detection at 1.4 GHz is burst B68-Wb with a reported fluence of 1587 Jy ms (or $E_\nu = 2.2^{+0.4}_{-0.4} \times 10^{32}$ erg Hz$^{-1}$). FAST is the most sensitive telescope currently operating at this wavelength range, with a completeness threshold of 54 mJy ms (H. Xu et al. 2022). B68-Wb would therefore still been detected by FAST if FRB 20220912Awould have been at a redshift of $z = 9.9^{+1.1}_{-1.1}$ and the burst was emitted at ∼14 GHz.

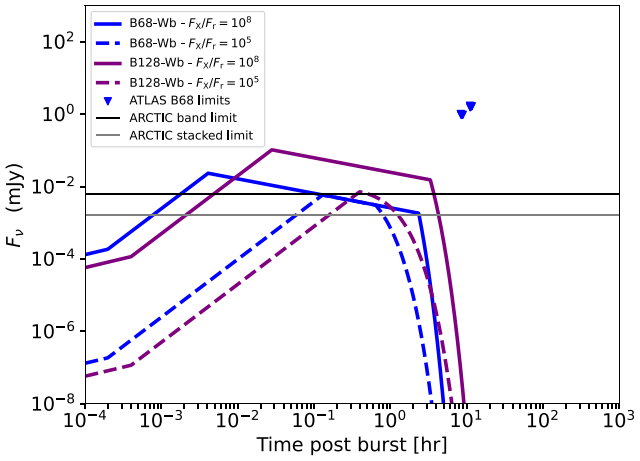


**Figure 6.** Predicted optical afterglows for maser shock model. The predicted optical afterglow from B68-Wb and B128-Wb in the synchrotron maser model framework (A. J. Cooper et al. 2022). We also show $5\sigma$ limits obtained by the ATLAS telescope network from 8 h after B68-Wb, and include typical limiting magnitudes from the ARCTIC telescope which could have been achieved if observations were scheduled rapidly after B68-Wb and B128-Wb (C. D. Kilpatrick et al. 2021).

At 330 MHz our brightest detection is burst B128-Wb with a measured fluence of 2629 Jy ms (or $E_\nu = 3.6^{+0.7}_{-0.7} \times 10^{32}$ erg Hz$^{-1}$). With the reported detection limit of CHIME/FRB of 1 Jy ms (R. Mckinven & CHIME/FRB Collaboration 2022), burst B128-Wb would still have been observable if the source was placed at redshift $z = 2.8^{+0.3}_{-0.3}$ with an implied emitting frequency of ∼1.2 GHz. Although the majority of CHIME sources do not have measured redshifts, their highest measured DM source, FRB 20180906B, is consistent with originating in the aforementioned redshift range with an estimated redshift of $z = 2.95$ (P. Chawla et al. 2022). CHIME is not detecting a large population of these high-redshift sources (K. Shin et al. 2023). This could be related to the large scattering for high-redshift FRBs ($z > 1$) at the observing frequency of CHIME (S. K. Ocker et al. 2022).

These high-energy bursts, emitted at high redshift, could potentially be observed by future telescopes with good field-of-view (FoV) and increased sensitivity, such as CHORD (K. Vanderlinde et al. 2019). Upcoming radio telescopes with extremely large FoV but lower sensitivity, such as BURSTT (FoV ∼ $10^4$ deg$^2$; H.-H. Lin et al. 2022), will accumulate a large number of observing hours on repeating sources like FRB 20220912A and probe the high-energy burst distribution. Furthermore, these events could also be detected in the far side lobes of CHIME/FRB (H.-H. Lin et al. 2024).

## 5 CONCLUSIONS

We conducted a high-cadence observational campaign towards FRB 20220912A spanning 117 d for a total of 2192 h between 2022 October and 2023 February. We detected a total of 130 high-energy FRBs ($\mathcal{F} > 10$ Jy ms). Of these, 114 unique bursts were detected at 1.4 GHz ($L$ band) and we detected 16 bursts at 330 MHz ($P$ band). Our main conclusions can be summarized as:

(i) We observe a break ($E_\nu^{\rm break} \sim 3.2 \times 10^{30}$ erg Hz$^{-1}$) in the cumulative burst energy distribution with a flattening of the power-law slope at higher energies. Interestingly, a similar break has been

Downloaded from academic.oup.com/mnras/article/545/2/staf1937/8317171 by Universiteit van Amsterdam user on 09 October 2026

observed in the energy distribution of FRB 20201124A by F. Kirsten et al. (2024).

(ii) We find a characteristic maximum energy at $E_\nu^{\rm char} = 2.09^{+3.78}_{-1.04} \times 10^{32}$ erg Hz$^{-1}$ or, equivalently, a total energy $\log_{10}(E^{\rm char}) = 41.32^{+0.45}_{-0.30}$ erg. This value is consistent with measurements of the characteristic energy for different population studies of apparently one-off FRBs which range between $\log_{10}(E^{\rm char}) = 41.26$–$42.08$ erg (Table 3). This could suggest a common physical mechanism for the emission of repeating and non-repeating FRB sources. Furthermore, we find that the integrated energy release above and below the break are approximately equal.

(iii) When it was active, FRB 20220912A contributed significantly to the all-sky FRB rate: $7.3^{+2.4}_{-1.9}$ per cent $R_{\rm sky}(\mathcal{F} > 100$ Jy ms) and $22.0^{+15.6}_{-10.3}$ per cent $\rm R_{sky}(\mathcal{F} > 500$ Jy ms). This fraction of the all-sky FRB rate was almost an order of magnitude higher than that of the other well-characterized hyperactive repeating source, FRB 20201124A.

(iv) Based on the total observed radio energy at 1.4 GHz ($L$ band), we are able to estimate that the total magnetic energy of a typical magnetar would be depleted on a time-scale of $\tau \sim 2150$ h. This time-scale implies that the radio efficiency may be larger than $\epsilon_{\rm radio} \gg 10^{-5}$, the magnetic field may be $B \gg 10^{15}$ G, the external magnetic field is continuously replenished (e.g. via core field expulsion), or strong multipolar field components power most of the emitted energy.

(v) We find that FRB 20220912A can produce bursts that are energetic enough for optical telescopes to detect a fiducial afterglow of shock-based FRB models with prompt (<hour) follow-up (Fig. 6) and we show that the most energetic burst would have been detectable even if the source was at redshift $z = 9.9^{+1.1}_{-1.1}$, assuming that high-energy bursts are emitted at higher radio frequencies.

High-cadence monitoring totalling 100+ hours, not just telescope sensitivity, is essential for detecting the most bright and rare FRBs and revealing the high-energy tails of the energy distributions of (repeating) FRBs. Future observing campaigns similar to the one described in this work promise to provide additional insights on FRB sources and emission mechanisms.

## ACKNOWLEDGEMENTS

We thank the directors and staff of the participating telescopes for allowing us to observe with their facilities. We thank Willem van Straten for modifying the DSPSR software package to fit our needs and for helping us with the SPC-algorithm. We thank Phil Uttley for discussions regarding MCMC analysis and fitting of the energy distribution. This work makes use of data from the Westerbork Synthesis Radio Telescope owned by ASTRON. ASTRON, the Netherlands Institute for Radio Astronomy, is an institute of the Dutch Scientific Research Council NWO (Nederlandse Oranisatie voor Wetenschappelijk Onderzoek). We thank the Westerbork operators Richard Blaauw, Jurjen Sluman, and Henk Mulder for scheduling and supporting observations. This work is based in part on observations carried out using the 32-m radio telescope operated by the Institute of Astronomy of the Nicolaus Copernicus University in Toruń (Poland) and supported by a Polish Ministry of Science and Higher Education SpUB grant. We express our gratitude to the operators and observers of the Astropeiler Stockert telescope: Thomas Buchsteiner, Bert Engelskirchen, Elke Fischer, Hans-Peter Löge, Thomas Nitsche, and Kevin Schmitz. This work is supported by the NWO XS grant: WesterFlash (OCENW.XS22.1.053; PI: Kirsten). The AstroFlash research group at McGill University, University of Amsterdam, ASTRON, and JIVE is supported by: a Canada Excellence Research Chair in Transient Astrophysics (CERC-2022-00009); the European Research Council (ERC) under the European Union's Horizon 2020 research and innovation programme ('EuroFlash'; grant agreement no. 101098079); and an NWO-Vici grant ('AstroFlash'; VI.C.192.045). AJC acknowledges support from the Oxford Hintze Centre for Astrophysical Surveys which is funded through generous support from the Hintze Family Charitable Foundation. DH acknowledges support from NWO's Women In Science Excel (WISE) programme. FK acknowledges support from Onsala Space Observatory for the provisioning of its facilities/observational support. The Onsala Space Observatory national research infrastructure is funded through Swedish Research Council grant no. 2017–00648. KN is an MIT Kavli Fellow. ZP is supported by an NWO Veni fellowship (VI.Veni.222.295).

## DATA AVAILABILITY

The data supporting the plots and full analysis in this article and other findings of this study are available under https://doi.org/10.5281/zenodo.11261763. The scripts and Jupyter notebooks used to analyse the data, generate the plots and tables with the burst properties are available at https://github.com/astroflash-frb/frb20220912a-ouldboukattine-2025.

## REFERENCES

Agarwal D., Aggarwal K., Burke-Spolaor S., Lorimer D. R., Garver-Daniels N., 2020, MNRAS, 497, 1661
Alstott J., Bullmore E., Plenz D., 2014, PLoS ONE, 9, e85777
Barr E. D. et al., 2013, MNRAS, 435, 2234
Bera A., Chengalur J. N., 2019, MNRAS, 490, L12
Bhardwaj M. et al., 2021, ApJ, 910, L18
Bochenek C. D., Ravi V., Belov K. V., Hallinan G., Kocz J., Kulkarni S. R., McKenna D. L., 2020, Nature, 587, 59
CHIME/FRB Collaboration, 2020, Nature, 587, 54
CHIME/FRB Collaboration, 2023, ApJ, 947, 83
CHIME/FRB Collaboration, Andersen B. C., 2022, Nature, 607, 256
Chawla P. et al., 2022, ApJ, 927, 35
Cognard I., Shrauner J. A., Taylor J. H., Thorsett S. E., 1996, ApJ, 457, L81
Cooper A. J., Wijers R. A. M. J., 2021, MNRAS, 508, L32
Cooper A. J. et al., 2022, MNRAS, 517, 5483
Cordes J. M., McLaughlin M. A., 2003, ApJ, 596, 1142
Cordes J. M., Bhat N. D. R., Hankins T. H., McLaughlin M. A., Kern J., 2004, ApJ, 612, 375
Crawford D. F., Jauncey D. L., Murdoch H. S., 1970, ApJ, 162, 405
Foreman-Mackey D., 2016, J. Open Source Softw., 1, 24
Foreman-Mackey D., Hogg D. W., Lang D., Goodman J., 2013, PASP, 125, 306
Geyer M. et al., 2021, MNRAS, 505, 4468
Gordon A. C. et al., 2023, ApJ, 954, 80
Gourdji K., Michilli D., Spitler L. G., Hessels J. W. T., Seymour A., Cordes J. M., Chatterjee S., 2019, ApJ, 877, L19
Hewitt D. M. et al., 2023, MNRAS, 526, 2039
Hewitt D. M. et al., 2024, MNRAS, 529, 1814
Huehnerhoff J. et al., 2016, in Evans C. J., Simard L., Takami H., eds, Proc. SPIE Conf. Ser. Vol. 9908, Ground-based and Airborne Instrumentation for Astronomy VI. SPIE, Bellingham, p. 99085H
Ikebe S. et al., 2023, PASJ, 75, 199
James C. W., Ekers R. D., Macquart J. P., Bannister K. W., Shannon R. M., 2019, MNRAS, 483, 1342
James C. W., Prochaska J. X., Macquart J. P., North-Hickey F. O., Bannister K. W., Dunning A., 2022a, MNRAS, 509, 4775
James C. W. et al., 2022b, MNRAS, 516, 4862
Jenet F. A., Anderson S. B., 1998, PASP, 110, 1467
Kaspi V. M., Beloborodov A. M., 2017, ARA&A, 55, 261
Keimpema A. et al., 2015, Exp. Astron., 39, 259
Kilpatrick C. D. et al., 2021, ApJ, 907, L3



Downloaded from academic.oup.com/mnras/article/545/2/staf1937/8317171 by Universiteit van Amsterdam user on 09 October 2026

Kirsten F., Snelders M. P., Jenkins M., Nimmo K., van den Eijnden J., Hessels J. W. T., Gawroński M. P., Yang J., 2021, Nat. Astron., 5, 414
Kirsten F. et al., 2024, Nat. Astron., 8, 337
Konijn D. C. et al., 2024, MNRAS, 534, 3331
Kumar P., Bošnjak Ž., 2020, MNRAS, 494, 2385
Kumar P., Lu W., Bhattacharya M., 2017, MNRAS, 468, 2726
Li C. K. et al., 2021, Nat. Astron., 5, 378
Li D. et al., 2021, Nature, 598, 267
Lin H.-H. et al., 2022, PASP, 134, 094106
Lin H.-H. et al., 2024, ApJ, 975, 75
Lu W., Kumar P., 2019, MNRAS, 483, L93
Lu W., Piro A. L., 2019, ApJ, 883, 40
Lu W., Kumar P., Narayan R., 2019, MNRAS, 483, 359
Luo R., Men Y., Lee K., Wang W., Lorimer D. R., Zhang B., 2020, MNRAS, 494, 665
Lyutikov M., 2017, ApJ, 838, L13
Lyutikov M., Lorimer D. R., 2016, ApJ, 824, L18
Macquart J. P., Ekers R., 2018, MNRAS, 480, 4211
Margalit B., Beniamini P., Sridhar N., Metzger B. D., 2020, ApJ, 899, L27
McKee J. W. et al., 2019, MNRAS, 483, 4784
Mckinven R., CHIME/FRB Collaboration, 2022, Astron. Telegram, 15679, 1
Mereghetti S. et al., 2020, ApJ, 898, L29
Metzger B. D., Margalit B., Sironi L., 2019, MNRAS, 485, 4091
Mickaliger M. B. et al., 2012, ApJ, 760, 64
Nimmo K. et al., 2023, MNRAS, 520, 2281
Ocker S. K. et al., 2022, ApJ, 931, 87
Pearlman A. B. et al., 2025, Nat. Astron., 9, 111
Petroff E., Hessels J. W. T., Lorimer D. R., 2022, A&AR, 30, 2
Pleunis Z. et al., 2021, ApJ, 923, 1
Ransom S., 2011, Astrophysics Source Code Library, record ascl:1107.017
Ravi V., 2022a, Astron. Telegram, 15693, 1
Ravi V., 2022b, Astron. Telegram, 15716, 1
Ravi V. et al., 2022, MNRAS, 513, 982
Ravi V. et al., 2023, ApJ, 949, L3
Ridnaia A. et al., 2021, Nat. Astron., 5, 372
Ryder S. D. et al., 2023, Science, 382, 294
Schechter P., 1976, ApJ, 203, 297
Shannon R. M. et al., 2018, Nature, 562, 386
Sheikh S. Z. et al., 2024, MNRAS, 527, 10425
Shin K. et al., 2023, ApJ, 944, 105
Snelders M. P. et al., 2023, Nat. Astron., 7, 1486
Soglasnov V. A., Popov M. V., Bartel N., Cannon W., Novikov A. Y., Kondratiev V. I., Altunin V. I., 2004, ApJ, 616, 439
Spitler L. G. et al., 2016, Nature, 531, 202
van Straten W., Bailes M., 2011, Publ. Astron. Soc. Aust., 28, 1
Tavani M. et al., 2021, Nat. Astron., 5, 401
Tonry J. L. et al., 2018, PASP, 130, 064505
Vanderlinde K. et al., 2019, The Canadian Hydrogen Observatory and Radio-transient Detector (CHORD),
Wadiasingh Z., Beniamini P., Timokhin A., Baring M. G., van der Horst A. J., Harding A. K., Kazanas D., 2020, ApJ, 891, 82
Wang W.-Y., Xu R., Chen X., 2020, ApJ, 899, 109
Whitney A., Kettenis M., Phillips C., Sekido M., 2010, in Navarro R., Rogstad S., Goodhart C. E., Sigman E., Soriano M., Wang D., White L. A., Jacobs C. S., eds, Sixth International VLBI Service for Geodesy and Astronomy. Proceedings from the 2010 General Meeting. NASA, p. 192
Xu H. et al., 2022, Nature, 609, 685
Yang Y.-P., Zhang B., 2021, ApJ, 919, 89
Zhang J.-S. et al., 2025, preprint (arXiv:2507.14707)
Zhang Y.-K. et al., 2023, ApJ, 955, 142

## SUPPORTING INFORMATION

Supplementary data are available at *MNRAS* online.

**ouldboukattine_energetics_suppl_figures**
Please note: Oxford University Press is not responsible for the content or functionality of any supporting materials supplied by the authors. Any queries (other than missing material) should be directed to the corresponding author for the article.

## APPENDIX A: OBSERVATIONAL OVERVIEW

Observational overview of the FRB 20220912A observing campaign is provided in Fig. B1.

## APPENDIX B: BURST PROPERTIES

### B1 Dispersion measures

Applying this best-fitting DM on bursts detected at *P* band (330 MHz) leaves a residual dispersive sweep, as seen in Fig. B2. To find the best-fitting DM, we dedispersed the burst to a range of trial DM values ranging from 219.665 to 219.799 pc cm$^{-3}$ and measured the peak S/N value at each trial DM. We subsequently fitted a Gaussian to the S/N-DM curve and found a best-fitting DM value of 219.735 pc cm$^{-3}$, as shown in Fig. B2.

### B2 Digitization artefacts

We record voltage data at Westerbork, Onsala, and Toruń in 2-bit sampling mode. The low bit depth leads to a relatively modest data rate ($\sim$500 GB/h for $\Delta\nu \sim 128$ MHz), which allows us to observe at a high cadence and process the data with low latency. The downside of the 2-bit sampling, however, is the limited dynamic range of the samples. Digitization artefacts can manifest in the data in case the power of a burst is concentrated in both time and frequency, for example during strong scintillation (S. Ikebe et al. 2023; F. Kirsten et al. 2024). This effect can in turn result in underestimation of the energies of the bursts. We do not observe any digitization artefacts in the 32-bit data recorded by Stockert.

The behaviour and proposed treatment of digitization artefacts in 2-bit sampled data has been described by F. A. Jenet & S. B. Anderson (1998, see their section 4.1 and fig. 4). In essence, the 2-bit digitizer has a non-linear response to the received power, which causes the digitized signal to be underestimated compared with the total power of the un-digitized signal. This effect scales with the brightness of the signal and manifests itself as decreased power during the time of the bursts, especially during bright scintillation. This decreased power is visible as 'depressions' in the dynamic spectrum and 'dips' in the frequency-averaged time series before and after the burst. In our observing set-up, we quantise our data per subband, typically 8–32 MHz, with the result that the digitization artefacts do not span or affect the entire observing bandwidth but are limited per subband, as visible in the top three subbands for burst B68-Wb in Fig. 1.

One way to correct for the digitization artefacts is by using a dynamic level-setting scheme. This method will counter the 'depression' area around the signal, but a byproduct of this method is an increase of power around the signal, which is known as quantisation noise. When applying the dynamic level-setting this increase in power is scattered uniformly across the bandwidth (in our case across a subband). Therefore, the power of the signal will be artificially increased and overestimated. This effect is best visible in the time series of a burst where power is increased before and after the burst; see Extended Data fig. 4 in F. Kirsten et al. (2024).

To best estimate the power of a signal we therefore need to remove the scattered quantisation noise. This is done using a scattered power correction (SPC) algorithm, which has been implemented in the DSPSR software package and is applied on a per-subband basis for our recording set-up.

Downloaded from academic.oup.com/mnras/article/545/2/staf1937/8317171 by Universiteit van Amsterdam user on 09 October 2026

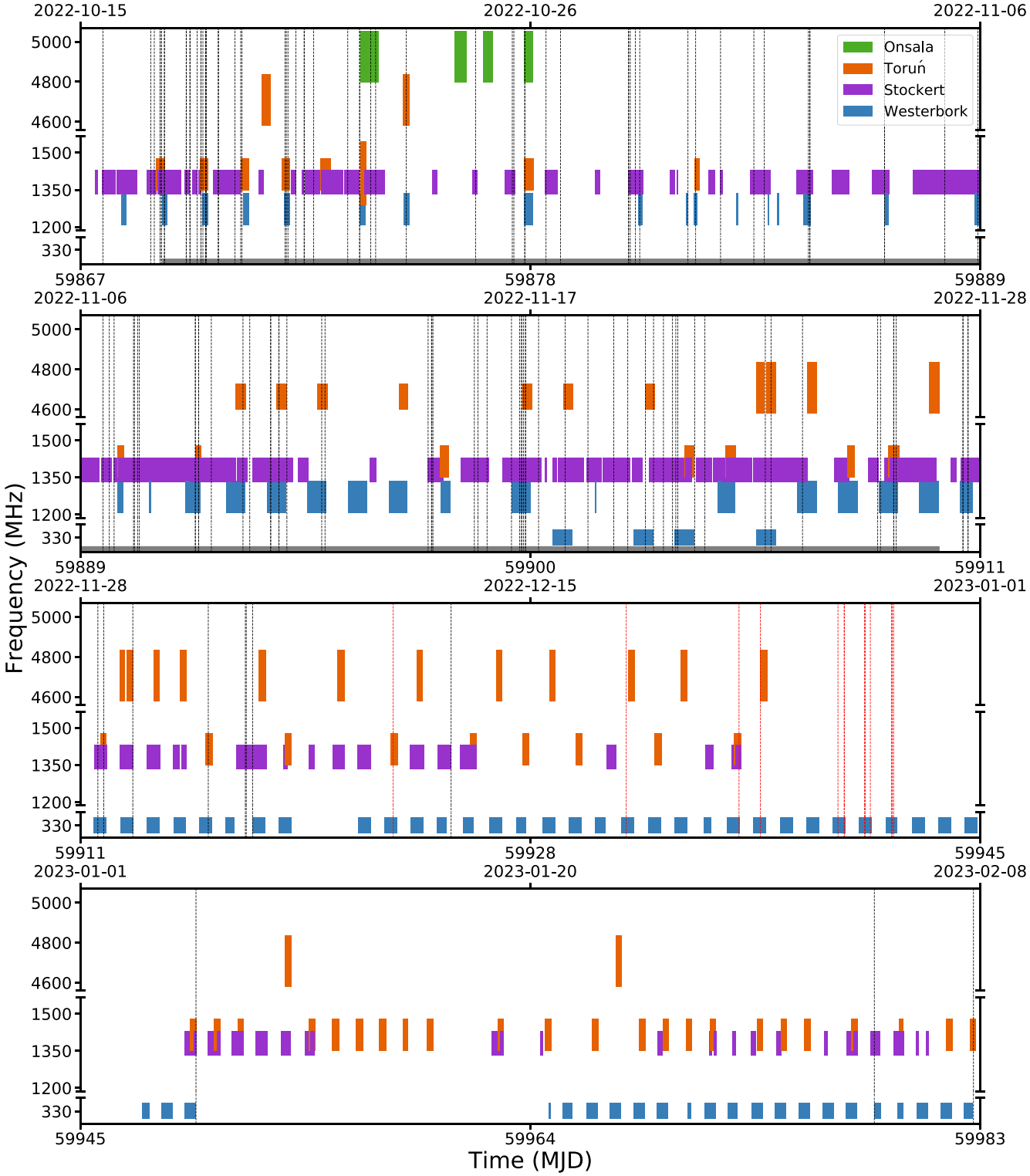


**Figure B1.** Overview of the FRB 20220912A observing campaign. Each coloured block represents an observation with a telescope at a certain frequency. The top two panels show 22 d and the bottom two panels show 36 d with the associated MJD and and calendar dates on the *x*-axis. The broken *y*-axis show the frequency range. The vertical dotted lines denote detections of bursts where black illustrates detections at *L* band (1.4 GHz) and red detections at *P* band (0.3 GHz). The bar in the top panels indicate the overlapping observing window with FAST and NRT.

We create three different data products, following the same methodology we employed in F. Kirsten et al. (2024). For Method I, we use the Super FX Correlator (SFXC). We coherently (within each frequency channel) and incoherently (between frequency channels) correct the data for dispersion (A. Keimpema et al. 2015). SFXC does not apply a dynamic level-setting scheme to the data, which means that the 'dips' and 'depressions' are still present in the data. Subsequently, for Method II we process the bursts using `digifil`,



Downloaded from academic.oup.com/mnras/article/545/2/staf1937/8317171 by Universiteit van Amsterdam user on 09 October 2026

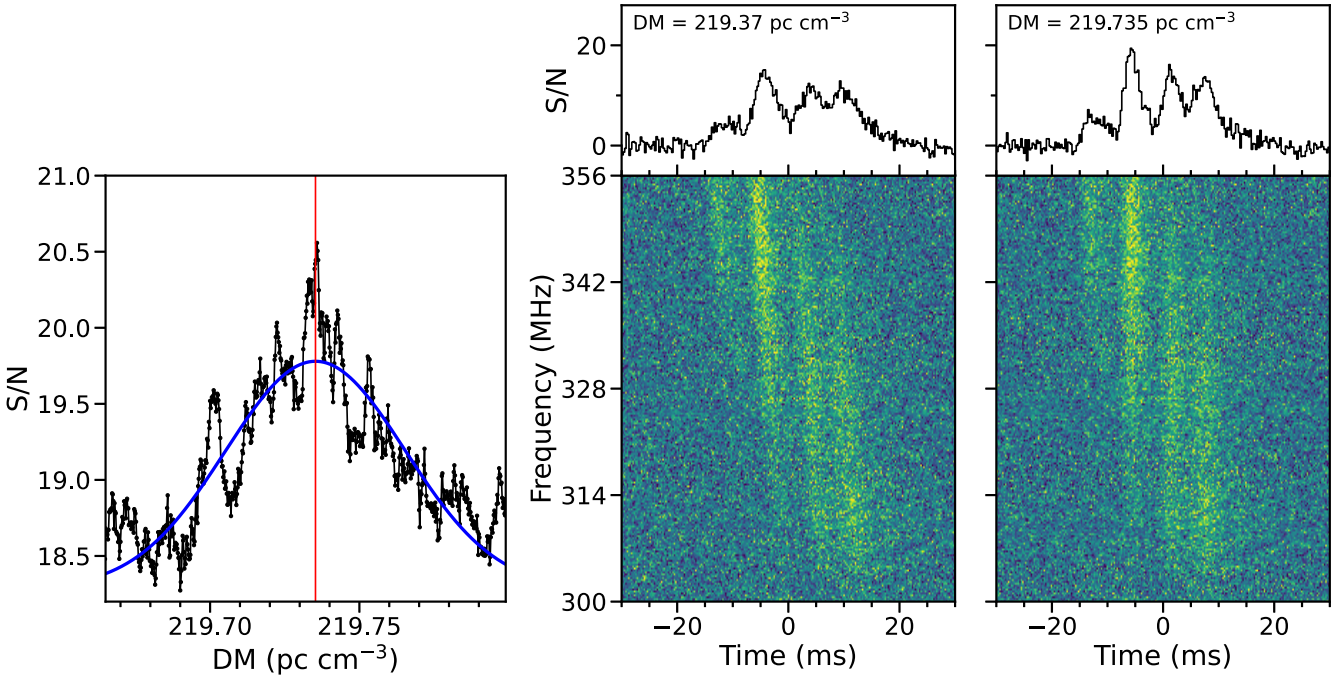


**Figure B2.** DM determination for bursts detected at *P* band. Peak SN versus DM curve for our brightest detection at *P* band, burst B128-Wb. When applying the DM used to correct for dispersive delay for bursts detected at *L* band, 219.37 pc cm$^{-3}$, there still was a residual sweep present for bursts detected at *P* band, as illustrated in the middle panel. By correcting the burst for range of DM values and fitting a Gaussian to the SN-curve we find a best-fitting DM of 219.375 pc cm$^{-3}$ and shown in the right panel.

which does apply dynamic level-setting and introduces quantisation noise. Lastly, for Method III we apply the SPC algorithm to the data products made using `digifil` in order to compensate for the quantisation noise.

In Fig. B3, we show the ratio of fluences relative to those measured using Method III for bursts detected at *L* band and *P* band. For *L* band, we find that applying Method I underestimates the fluences by up to 40 per cent, while Method II overestimates them by up to 10 per cent. For *P* band, these digitization effects are less apparent which is most likely due to the longer dispersive sweep of the burst and low sensitivity of the *P*-band receiver at Wb.

Downloaded from academic.oup.com/mnras/article/545/2/staf1937/8317171 by Universiteit van Amsterdam user on 09 October 2026

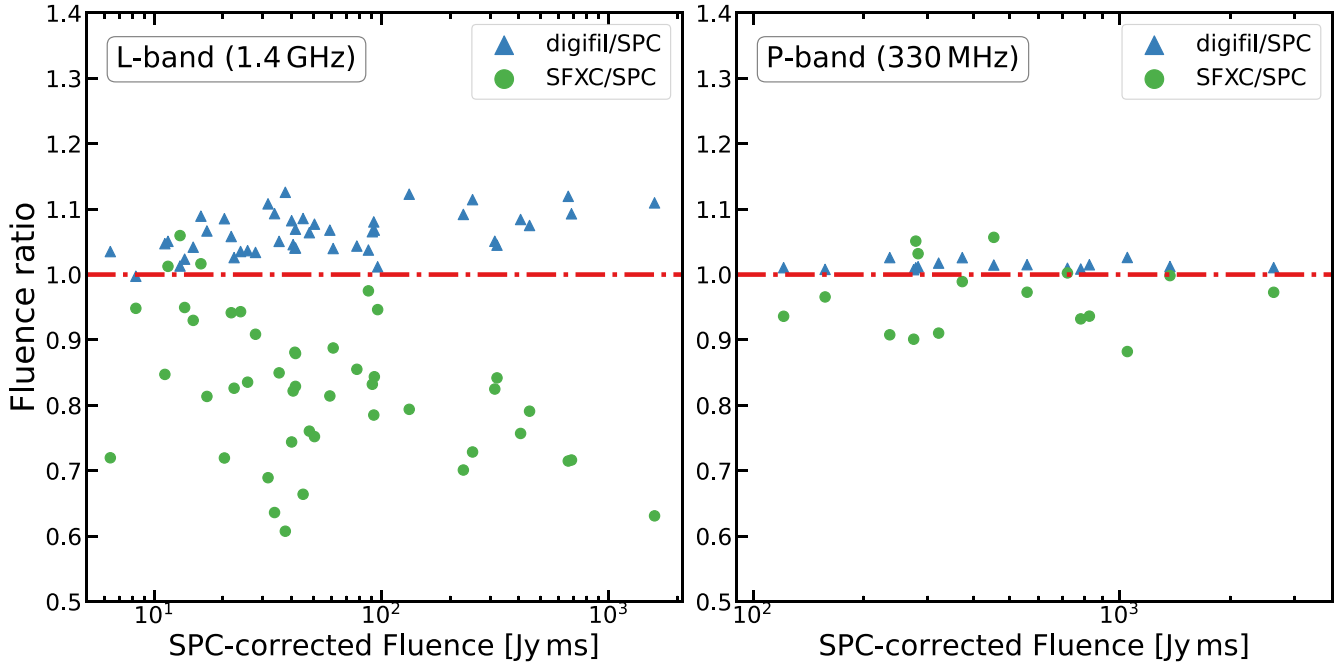


**Figure B3.** Ratio of fluences computed from SFXC- and digifil-generated filterbanks. The fluence for each burst was measured three different ways due to digitization artefacts present in the data. These filterbanks were made for bursts detected with Westerbork and Toruń using `SFXC`, `digifil`, and `digifil` with a scattered power correction (SPC) applied. Here, we plot the ratio of these measured fluences for *L* band (left panel) and *P* band (right panel). For *L* band, we find that due to digitization effects the fluence of the burst can be underestimated for up to 40 per cent (`SFXC`) and overestimated for 10 per cent (`digifil`). Applying the SPC algorithm to correct for digitization effects is therefore essential. Even though we detect bright (>1000 Jy ms) bursts at *P* band, these digitization effects are less apparent, this most likely due to longer dispersive sweep of the burst and the low sensitivity of the Westerbork *P*-band receiver.

This paper has been typeset from a TEX/LATEX file prepared by the author.

Downloaded from academic.oup.com/mnras/article/545/2/staf1937/8317171 by Universiteit van Amsterdam user on 09 October 2026

© The Author(s) 2025.
Published by Oxford University Press on behalf of Royal Astronomical Society. This is an Open Access article distributed under the terms of the Creative Commons Attribution License (https://creativecommons.org/licenses/by/4.0/), which permits unrestricted reuse, distribution, and reproduction in any medium, provided the original work is properly cited.